inorganics

MDPI

Review

RETRACTED: A Comprehensive Review of Recent Advances in Perovskite Materials: Electrical, Dielectric, and Magnetic Properties

Faouzia Tayari, Silvia Soreto Teixeira, Manuel Pedro F. Graca and Kais Iben Nassar *

I3N-Aveiro, Department of Physics, University of Aveiro, 3810-193 Aveiro, Portugal; faouzia.tayari@ua.pt (F.T.); silvia.soreto@ua.pt (S.S.T.); mpfg@ua.pt (M.P.F.G.)
* Correspondence: kais.nassar@ua.pt

Abstract: Perovskite materials have emerged as one of the most promising classes of compounds in recent years due to their unique combination of electrical, dielectric, and magnetic properties, which make them ideal candidates for a wide range of advanced technological applications. This comprehensive review explores the latest developments in the electrical, dielectric, and magnetic behavior of perovskites, providing an in-depth analysis of the underlying mechanisms and their potential for improving device performance. The review covers the fundamental aspects of charge transport, polarization, and magnetic interactions in perovskite structures including the impact of crystal symmetry, ion migration, and external stimuli on their properties. Moreover, it highlights the various strategies used to tailor these properties through compositional engineering, doping, and structural modifications, resulting in enhanced efficiency, stability, and multifunctionality in applications such as photovoltaics, capacitors, dielectric resonators, and spintronic devices. Additionally, the paper addresses the challenges associated with the practical implementation of perovskite materials including stability issues under harsh environmental conditions and scalability for industrial applications. The review concludes with an outlook on future directions, emphasizing the need for further research to overcome these challenges and unlock the full potential of perovskite materials in next-generation electronics, energy storage, and magnetic devices.

Keywords: perovskite; sol-gel route; impedance complex; electrical conductivity; dielectric relaxation; magnetic properties

check for updates

Academic Editors: Sake Wang, Nguyen Tuan Hung and Minglei Sun

Received: 29 November 2024
Revised: 21 February 2025
Accepted: 22 February 2025
Published: 24 February 2025
Retracted: 15 May 2026

Citation: Tayari, F.; Teixeira, S.S.; Graca, M.P.F.; Nassar, K.I. RETRACTED: A Comprehensive Review of Recent Advances in Perovskite Materials: Electrical, Dielectric, and Magnetic Properties. *Inorganics* **2025**, *13*, 67. https://doi.org/10.3390/inorganics13030067

Copyright: © 2025 by the authors. Licensee MDPI, Basel, Switzerland. This article is an open access article distributed under the terms and conditions of the Creative Commons Attribution (CC BY) license (https://creativecommons.org/licenses/by/4.0/).

1. Introduction

Perovskite materials, named after the mineral calcium titanate ($CaTiO_3$), have garnered immense attention due to their extraordinary structural versatility and remarkable functional properties. With a general formula of ABX_3, where 'A' and 'B' represent cations of differing sizes and 'X' is an anion, typically oxygen or halide, perovskites exhibit a wide range of tunable properties that are invaluable for modern technological applications. The flexibility of the perovskite structure, stemming from the diverse choices for A, B, and X components, allows for intricate tailoring of their electrical, dielectric, and magnetic properties, making them a cornerstone in materials science research [1–6].

The general formula for perovskites is ABX_3, where 'A' and 'B' are cations of differing sizes and 'X' is an anion that bonds to both. Typically, 'A' is a larger cation such as a rare-earth or alkaline-earth metal, 'B' is a smaller transition metal cation, and 'X' is an anion like oxygen [7–11]. This structure allows for a vast array of elemental substitutions, resulting in a rich variety of physical properties including notable magnetic behaviors [11–15]. The

This paper has been retracted. A retraction notice was published on 15 May 2026 in *Inorganics* **2026**, *14*, 134. https://doi.org/10.3390/inorganics14050134

RETRACTED

perovskite structure is characterized by a three-dimensional framework of corner-sharing BX_6 octahedra, with the 'A' cations occupying the interstitial sites [14–19]. This unique architecture not only stabilizes the structure, but also enables diverse magnetic interactions, driven by the intricate electronic correlations between the 'A' and 'B' site cations and anions [20–22]. The flexibility in the perovskite composition allows for the fine-tuning of these interactions, leading to phenomena such as ferroelectricity, magnetoresistance, magnetocaloric effects, and spintronics applications.

The structural and chemical aspects of perovskites play a critical role in dictating their physical properties. The ability to accommodate various ions in the A and B sites results in a vast library of perovskite compounds with distinct features. Structural distortions, such as tilting of the BX_6 octahedra, influence key parameters such as bandgap, ferroelectricity, and magnetic interactions. Furthermore, advancements in synthesis techniques have enabled precise control over compositional engineering, defect management, and nanostructuring, opening avenues for enhancing their performance in practical applications [23–25]. Since then, the study of perovskites has evolved significantly, particularly in the latter half of the 20th century with the advent of high-resolution characterization techniques and advanced synthesis methods. These advancements have enabled researchers to unravel the complex magnetic behaviors exhibited by perovskites, spurring a wave of innovations in both fundamental research and practical applications.

In terms of electrical and dielectric properties, perovskites have shown unprecedented potential in applications such as capacitors, energy storage devices, and piezoelectric sensors. Their ability to exhibit high dielectric constants, ferroelectricity, and ion conductivity makes them highly versatile for both fundamental research and industrial applications. The interplay between structural features and electronic behavior, including ion migration and polarization dynamics, has been a central theme in understanding and optimizing these properties. Similarly, perovskites have demonstrated unique magnetic properties, including ferromagnetism, antiferromagnetism, and spin-glass behavior, which are highly dependent on their composition and structural ordering. These properties are critical for spintronic applications, magnetic sensors, and data storage devices. The coupling between magnetic ordering and other functionalities, such as ferroelectricity in multiferroic perovskites, provides exciting opportunities for multifunctional device integration [26–28].

Ferroelectricity: Ferroelectric perovskites, such as $BaTiO_3$, exhibit spontaneous electric polarization that can be reversed by the application of an external electric field. This property is intimately linked with the material's crystal structure, where the displacement of the B-site cation relative to the anions creates a dipole moment [29–34]. The coupling between ferroelectricity and magnetism in certain perovskites has led to the discovery of multiferroic materials, which hold promise for novel electronic devices that exploit both electric and magnetic orderings.

Magnetoresistance: The phenomenon of magnetoresistance, where a material's electrical resistance changes in response to an applied magnetic field, is particularly pronounced in perovskite manganites [35–41]. This colossal magnetoresistance (CMR) effect is a consequence of the interplay between the electronic structure and magnetic ordering, driven by the double exchange mechanism. CMR materials are being explored for their potential in magnetic field sensors and spintronic devices.

Magnetocaloric effect: The magnetocaloric effect (MCE), which refers to the change in temperature of a material upon the application or removal of a magnetic field, is another intriguing property of perovskites. Materials exhibiting a large MCE are of great interest for magnetic refrigeration technologies, which offer an energy-efficient and environmentally friendly alternative to conventional gas-compression refrigeration. Perovskites such as

RETRACTED

$La(Fe, Si)_{13}$-based compounds have shown significant potential in this area, prompting ongoing research into optimizing their MCE for practical applications [42–46].

Spintronics and magnetochemistry: Spintronics, or spin-based electronics, represents a burgeoning field where the spin of electrons, in addition to their charge, is utilized for information processing. Perovskites play a crucial role in this domain due to their ability to exhibit spin-polarized currents and giant magnetoresistance. The interplay between the spin degrees of freedom and the lattice structure in perovskites enables the development of spintronic devices with enhanced functionality and performance [47–52]. Magnetochemistry, which explores the chemical aspects of magnetic materials, benefits greatly from the study of perovskites. The tunable nature of the perovskite structure allows for systematic investigations into how chemical substitutions and modifications affect magnetic properties. This understanding is crucial for designing materials with specific magnetic behaviors tailored for applications in catalysis, sensing, and magnetic data storage [53–57].

Applications and future directions: The diverse magnetic properties of perovskites have led to their incorporation into various applications. In addition to the aforementioned uses in sensors, memory devices, and refrigeration, perovskites are being explored for use in energy conversion and storage [58–61] as well as in biomedical applications such as magnetic resonance imaging (MRI) contrast agents and targeted drug delivery systems [59–69]. Despite the significant progress made in understanding and utilizing the magnetic properties of perovskites, several challenges remain. These include improving the stability and reproducibility of perovskite materials, enhancing their performance at room temperature, and developing scalable synthesis methods for industrial applications. Future research efforts are likely to focus on addressing these challenges as well as exploring new compositions and structures to unlock further potential in this versatile class of materials. The study of magnetic properties in perovskite materials is a dynamic and rapidly evolving field, driven by the unique structural characteristics and tunable nature of these compounds. Figure 1 illustrates the trends in publications related to perovskite materials, highlighting significant growth in the fields of electrical, dielectric, and magnetic properties. The data showed a consistent increase in research activity across all categories, underscoring the growing interest and advancements in these key areas of perovskite material applications. In addition to their diverse applications in sensors, memory devices, energy conversion, and biomedical fields, perovskite-based materials also show great promise for next-generation optoelectronic applications, particularly in light-emitting devices, which are expected to drive future innovations in the field [70].

This review aims to provide a comprehensive overview of the recent advances in the study of perovskite materials, with a focus on the structural and chemical aspects that underlie their diverse functional properties. It delves into the structural and chemical fundamentals of perovskites, discussing their crystalline frameworks, chemical tunability, and defect management and highlights their electrical and dielectric properties, emphasizing the mechanisms of charge transport, polarization, and dielectric behavior. It explores the magnetic properties of perovskites, discussing the key factors influencing their magnetic ordering and their implications for technological applications. The review concludes with a discussion of the challenges and future directions in the field, aiming to inspire further research into the design and application of perovskite materials.

RETRACTED

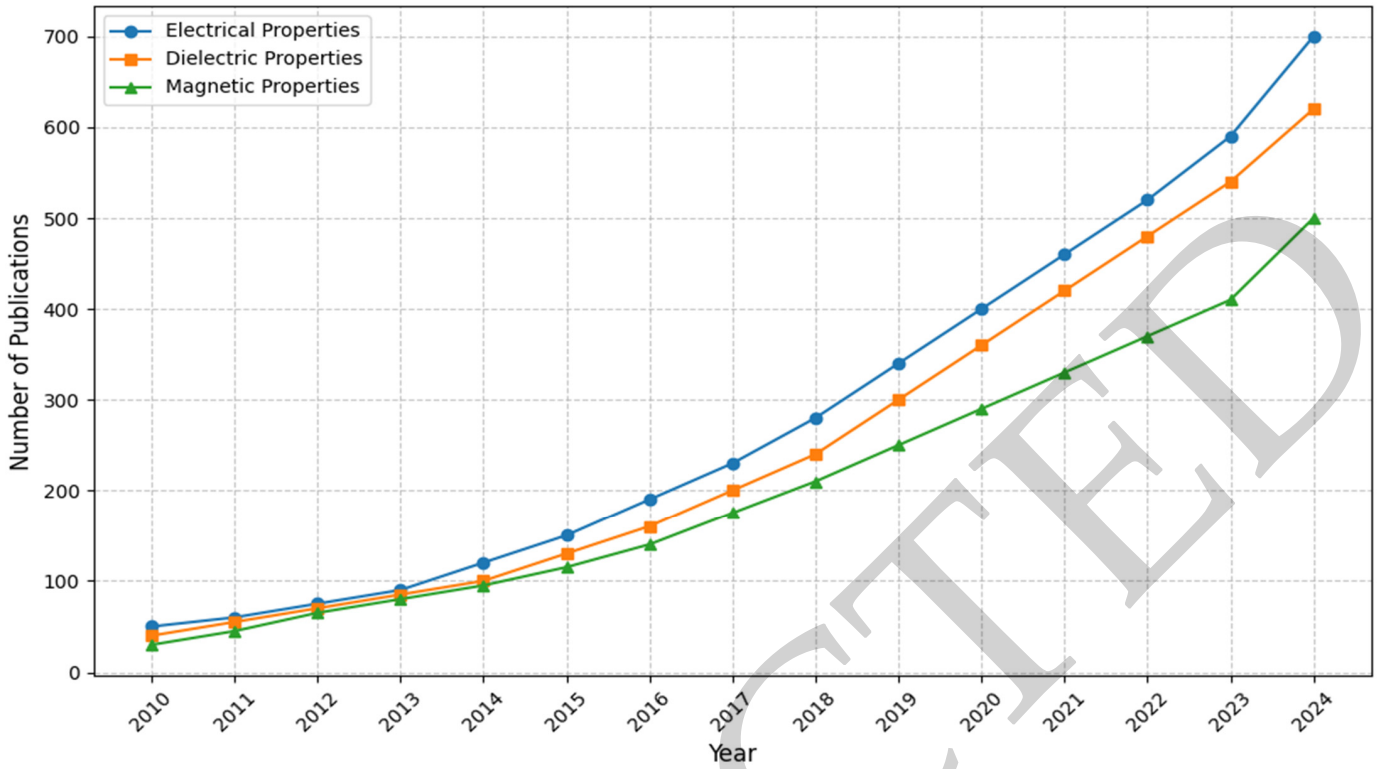


Figure 1. Trends in publications on perovskite materials highlighting electrical, dielectric, and magnetic properties.

2. Structural and Chemical Aspects of Perovskites

Perovskite materials, characterized by their ABX_3 crystal structure, exhibit a remarkable diversity in their chemical compositions and structural variations. Understanding the structural and chemical aspects is fundamental to elucidating their magnetic properties and exploring their potential applications across various fields (Figure 2).

Crystal structure and symmetry: The perovskite crystal structure consists of a three-dimensional network of corner-sharing BX_6 octahedra, where 'B' cations occupy the octahedral centers and 'X' anions reside at the vertices (Figure 3) [71,72]. The 'A' cations occupy the larger cubic sites between the octahedra. This arrangement gives rise to the general formula ABX_3, where 'A' is typically a larger cation (e.g., La, Ba) occupying the A-site, 'B' is a smaller transition metal cation (e.g., Ti, Mn) at the B-site, and 'X' is an anion (e.g., O, F) bonding to both 'A' and 'B'. The cubic perovskite structure (space group $Pm3^{-}m$) is stable under ambient conditions for many materials but can undergo distortions and phase transitions under different temperatures, pressures, or upon chemical substitution. These structural variations are crucial as they strongly influence the material's magnetic and electrical properties.

A-site and B-site cation substitutions: One of the defining features of perovskites is their ability to substitute both the 'A' and 'B' cations, leading to a vast array of materials with tailored properties. Substituting 'A'-site cations can influence lattice parameters, stability, and sometimes introduce charge carriers through doping. For instance, replacing La with Ca in $LaMnO_3$ can modify the material's magnetic and electronic properties. Similarly, B'-site cation substitutions can alter magnetic interactions and electronic configurations within the octahedral framework. This flexibility allows researchers to fine-tune properties such as magnetism, ferroelectricity, and conductivity. For example, replacing Mn with Fe or Co in perovskite manganites can significantly affect the magnetic ordering and magneto resistive behavior due to changes in the electronic structure and spin configurations. To

RETRACTED

gain deeper insights into charge generation and transfer within perovskite crystals, ultrafast laser transient absorption spectroscopy (TAS) serves as a valuable figure of merit tool. This technique is crucial for understanding the dynamics of charge carriers, which strongly correlate with the performance of perovskite-based devices [73,74].

Influence of anion (X) variations: The choice of anion in perovskite compounds also plays a critical role in determining their properties. Oxygen (O) is the most common anion in traditional perovskites, but other halides (e.g., F, Cl) or mixed anions can be incorporated to modify properties such as bandgap, conductivity, and magnetic ordering. Mixed-anion perovskites, like $BaZr_{(1-x)}$ $TixO_3$ or $LaMnO_{3-x}F_x$, exhibit intriguing properties that combine the characteristics of their constituent anions, offering new avenues for material design and applications.

Synthesis methods and techniques: The synthesis of perovskite materials is a pivotal aspect in controlling their structural and chemical properties (Figure 4). Various synthesis techniques, including solid-state reactions, sol-gel methods, chemical vapor deposition (CVD), and hydrothermal synthesis, offer different levels of control over particle size, crystallinity, and composition. Characterization techniques such as X-ray diffraction (XRD), scanning electron microscopy (SEM), transmission electron microscopy (TEM), and spectroscopic methods (e.g., X-ray photoelectron spectroscopy, Raman spectroscopy) are essential for elucidating the crystal structure, phase purity, and chemical composition of perovskite materials [75]. These techniques provide insights into how structural and chemical modifications impact the magnetic behaviors and overall performance of perovskite-based devices. The structural and chemical aspects of perovskite materials are pivotal in understanding their magnetic properties and tailoring them for specific applications. By manipulating the composition, doping, and synthesis conditions, researchers can unlock new functionalities and enhance the performance of perovskite materials in fields ranging from electronics and magnetism to energy conversion and beyond. Future research efforts will continue to explore novel compositions and synthesis strategies to further expand the capabilities of perovskite-based materials in emerging technologies.

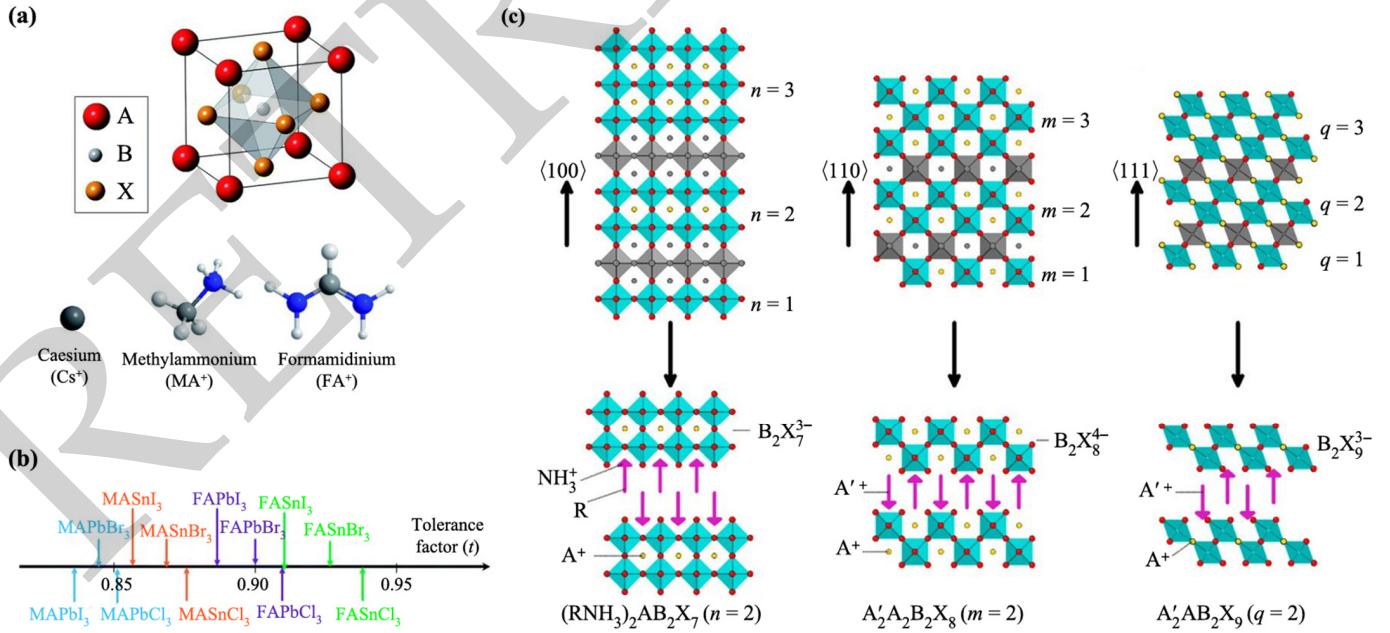


Figure 2. (**a**) Crystal structure of 3D perovskite ABX_3 with Cs^+, MA^+, or FA^+ cations. (**b**) Tolerance factors (t) of 3D halide perovskites. (**c**) Structure derivation of layered 2D perovskite with long cations cutting the 3D perovskite along the (100), (110), and (111) planes. Reproduced with permission from [76]. Copyright © 2019, Springer Nature.

RETRACTED

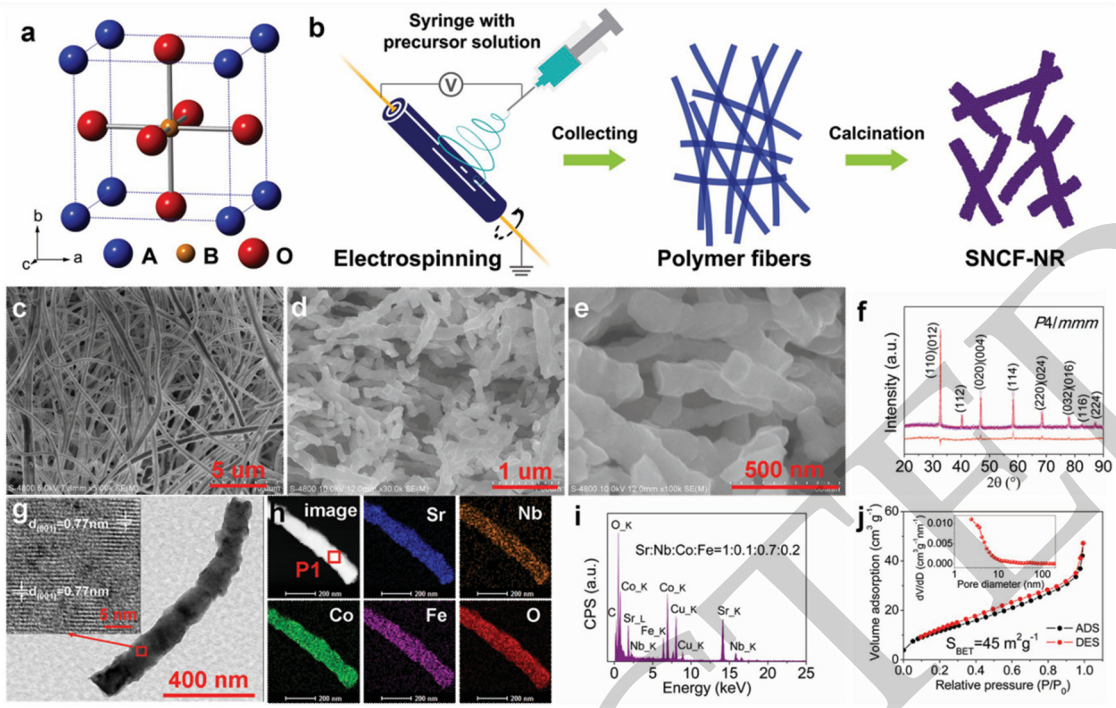


Figure 3. Structural and morphological insights into perovskite materials and solar cells. Reprinted with permission [77]. Copyright © 2017 Wiley-VCH Verlag GmbH & Co. KGaA, Weinheim.

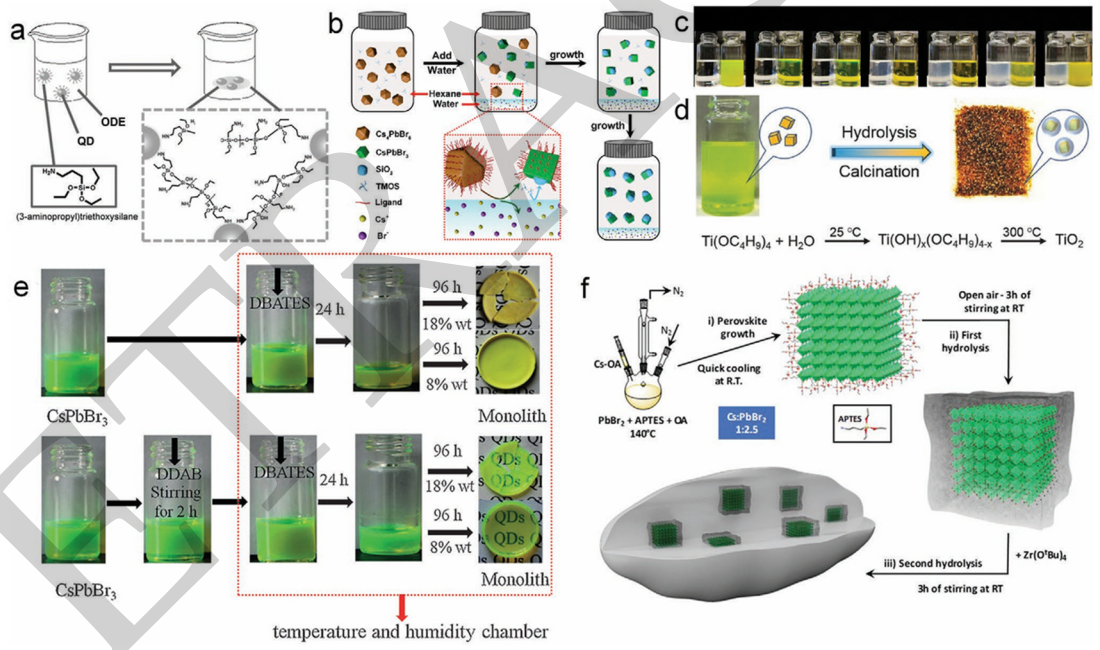


Figure 4. Synthesis (sol-gel) of perovskites. Reprinted with permission from Duan, Y., Wang, D., and Costa, R. D [78]. Copyright © 2021 Wiley-VCH Verlag GmbH & Co. KGaA, Weinheim.

Characterization Techniques

Characterizing perovskite materials is essential for understanding their structural, optical, electrical, and magnetic properties. Key characterization techniques include X-ray diffraction (XRD), which determines the crystal structure and phase purity of perovskite materials. Scanning electron microscopy (SEM) and transmission electron microscopy (TEM) provide detailed morphological and microstructural information at the nanoscale. Spectroscopic techniques including UV-Vis spectroscopy, Fourier-transform infrared spectroscopy (FTIR), and Raman spectroscopy analyze optical and vibrational properties. Electrical and

RETRACTED

magnetic measurements, such as Hall effect measurements, electrical conductivity, and magnetization measurements, probe electronic and magnetic properties [79–90].

3. Electrical and Dielectric Properties

Perovskite materials exhibit a fascinating array of electrical, dielectric, and magnetic properties, which are central to their widespread application in diverse technological fields. This section explores these properties in detail and discusses the role of impedance spectroscopy in understanding their complex behavior [91–95].

3.1. Electrical Properties

Perovskite materials demonstrate a wide range of electrical behaviors, spanning from insulation to metallic and superconducting states. This variability arises from the ability to finely tune their electronic structure through doping, compositional variations, and defect engineering. Understanding and controlling the electrical conductivity of perovskites are crucial for applications in electronic devices such as transistors, sensors, and energy storage systems. Recent breakthroughs in perovskite solar cells (PSCs) highlight their potential for achieving high efficiency and stability, promising advancements in renewable energy technologies. Achary et al. [96]. conducted a comprehensive study on the structural, electrical, and dielectric properties of two lead-free double perovskites, $BiHoZnZrO_6$ (BHZZR) and $BiHoCuTiO_6$ (BHCTO), synthesized using a cost-effective solid-state reaction technique. Their research revealed that substituting the pair of elements Zn and Zr with Cu and Ti induces a structural transition from a monoclinic to an orthorhombic crystal system (Figure 5). Microscopic imaging and energy-dispersive spectra confirmed the homogeneous distribution of grains and the formation of the desired compounds in both perovskites. Detailed impedance spectroscopy studies highlighted that the dielectric and electrical properties of these materials are significantly influenced by frequency and temperature variations [97–100].

It was observed that the grains, grain boundaries, and electrodes profoundly impact these properties, providing insights into the electrical conduction mechanisms and microstructural behaviors. Equivalent circuit models were developed to$_6$ extract electrical parameters such as bulk and grain boundary resistance and capacitance, facilitating a detailed comparison of the AC conductivity, electrical modulus, and transport properties of BHZZR and BHCTO. In examining the dielectric properties, the study focused on the dielectric loss (tan δ), which is the ratio of the real and imaginary parts of a capacitor's impedance at a given frequency. A higher tan δ indicates substantial dielectric absorption [101–104]. For capacitors constructed with lossy dielectrics, capacitance (C) changes more significantly with frequency, whereas good dielectric materials exhibit slower changes in C. The dielectric constant (ε_r) was defined as the ratio of a capacitor's capacity with BHZZR as the dielectric medium to that with a vacuum as the dielectric medium. The dielectric constant is temperature and frequency-dependent and was calculated using the formula $\varepsilon_r = Cp/C_0$, where C_p is the parallel capacitance obtained from impedance analysis, and C_0 is determined from the physical dimensions of the sample [105]. For instance, with a pellet diameter of 1.191 cm and thickness of 0.2295 cm, the calculated area was 1.113508×10^{-4} m^2, resulting in a C_0 value of 0.43 pF. Using this value, the dielectric constant was computed from the C_p data derived from the impedance results. The plots of dielectric constant versus frequency for BHZZR and BHCTO showed that the εr was initially high but decreased with increasing frequency for both samples. This behavior is influenced by interfacial, dipolar, ionic, atomic, and electronic polarizations. At lower frequencies, dipoles struggle to align with the alternating electric field, leading to higher dielectric constants. However, at higher frequencies, electronic polarization predominates,

RETRACTED

causing the dielectric constant to decline. This study elucidates the complex interplay between structural modifications and the resulting electrical and dielectric properties, offering valuable insights for the development and optimization of perovskite-based materials in various technological applications [106].

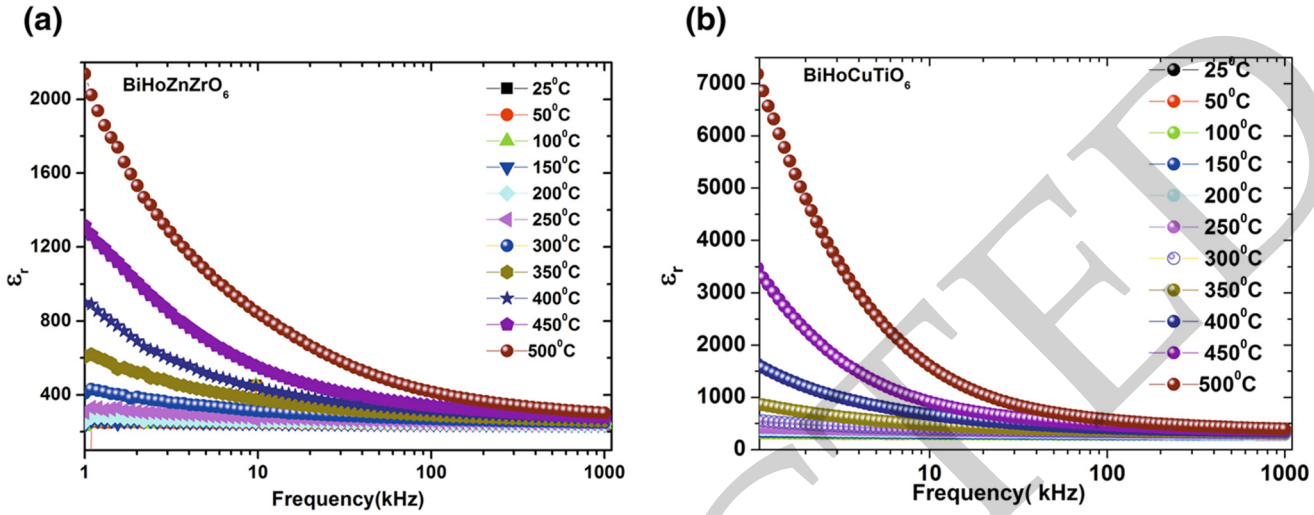


Figure 5. (**a**) The plot of dielectric constant with frequency for BHZZR. (**b**) The plot of dielectric constant with frequency for BHCTO. Reprinted with permission from Achary, P. G. R. et al. (2018) [106]. Copyright © 2018 Springer Science Business Media, LLC, part of Springer Nature.

In addition, Nassar et al. [107]. conducted an in-depth investigation into the AC electrical conductivity and dielectric properties of the double perovskite oxide $BiBaFeZnO_6$ (BiBFZO), synthesized using the sol-gel method. Their structural analysis revealed that BiBFZO crystallizes in a rhombohedral system with the R-3C space group, confirming its single-phase nature. The study employed impedance spectroscopy to examine the dielectric behavior and physical phenomena of the material over a temperature range of 200 to 380 K and frequencies up to 1 MHz. Nyquist diagrams at various temperatures displayed a flat semi-circular arc, modeled using an equivalent circuit comprising an RC element and an RQ element. The frequency-dependent behavior of the imaginary component of impedance (Z″) indicated a relaxation process, while electrical conductivity analysis, based on Jonscher's law, enabled the calculation of activation energy [108–110]. The results validated the non-overlapping small polaron tunneling (NSPT) model as a suitable explanation for the electrical conduction mechanism in BiBFZO. Electrical conductivity exhibited two distinct regions: a low-frequency region where conductivity remained constant, and a high-frequency region where the conductivity increased with frequency. The temperature-dependent variation in conductivity showed a linear behavior, indicative of a thermally activated transport mechanism. The dielectric properties of BiBFZO were also temperature and frequency-dependent (Figure 6). The complex impedance spectra showed a single flat semi-circular arc, which was interpreted using an equivalent circuit model comprising a constant phase element impedance (RQ element) and a parallel resistance-capacitance network (R_1-CPE_1 and R_2-C_1). Activation energy values obtained from both electrical conductivity and complex impedance measurements were found to be very similar, suggesting that the relaxation mechanism is attributable to the same type of charge carriers [111–115]. The temperature dependence of the exponents provided further insight into the conduction mechanism, supporting the NSPT model as the most appropriate for explaining the electrical conduction phenomena in BiBFZO.

RETRACTED

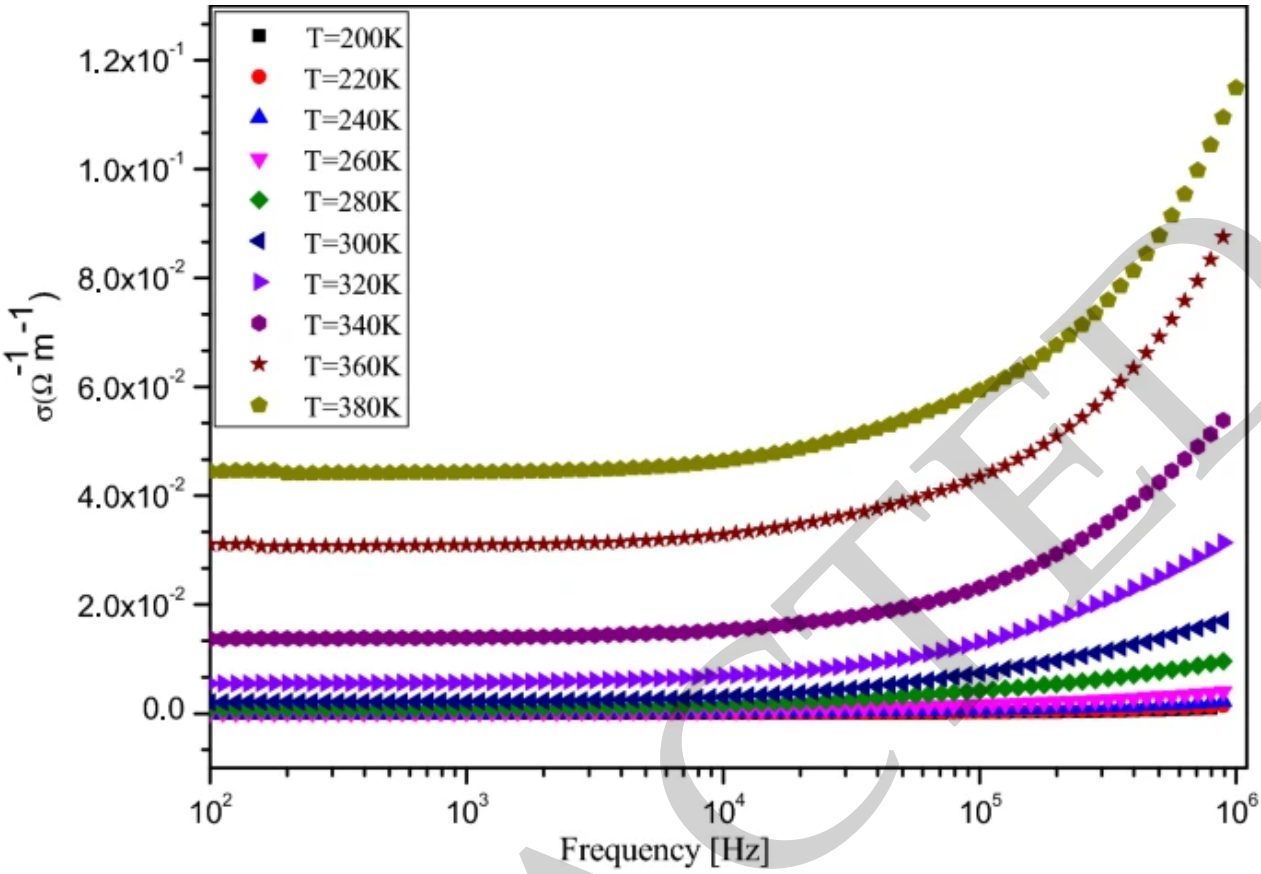


Figure 6. Frequency dependency of conductivity σ_{ac} for $BiBaFeZnO_6$. Reprinted with permission from Nassar, K. I. et al. [107]. Copyright © 2021 The Author(s), under exclusive license to Springer Science Business Media, LLC, part of Springer Nature.

Furthermore, K. Iben Nassar and colleagues [116] conducted an in-depth investigation into the structural and electrical properties of the double perovskite oxide $LaPbFeTiO_6$, synthesized using the sol-gel method. X-ray diffraction analysis revealed that $LaPbFeTiO_6$ crystallizes in the rhombohedral system with the space group R3C. The chemical composition and morphology of the grain size were confirmed through energy-dispersive spectroscopy (EDS) and scanning electron microscopy (SEM), respectively. Electrical conductivity and dielectric characterizations were performed as functions of frequency and temperature (ranging from 200 to 380 K) using impedance spectroscopy. Their results indicated that the dielectric constant of $LaPbFeTiO_6$ increased with temperature. In their study of AC conductivity, the frequency dependence was found to adhere to Jonscher's power law, where $\sigma(\omega) = \sigma_{DC} + A\omega^s$, with ω being the angular frequency, σ_{DC} is the DC conductivity, A is a constant, and s represents the interaction between mobile ions and surrounding lattices. The conductivity curves showed two distinct regions: a low-frequency plateau representing DC conductivity, and a high-frequency region where AC conductivity increased with frequency. This behavior suggests a thermally activated charge carrier hopping process, which intensifies with temperature [4,117–120]. The high-frequency conductivity variation, attributed to the relaxation phenomenon, is due to the mobility of charge carriers, implying their displacement from their original positions to new sites.

The experimental data fitting, performed using ORIGIN 8.0 software, confirmed these observations and indicated that $LaPbFeTiO_6$ behaves as a semiconductive material. Additionally, the temperature dependence of DC conductivity followed Arrhenius behavior, where the activation energy (E_a) was derived from the linear relationship between $Ln(\sigma_{DC})$

RETRACTED

and the inverse of temperature (1000/T) (see Figure 7). This analysis provided insights into the thermal activation energies and the conduction mechanisms in this material.

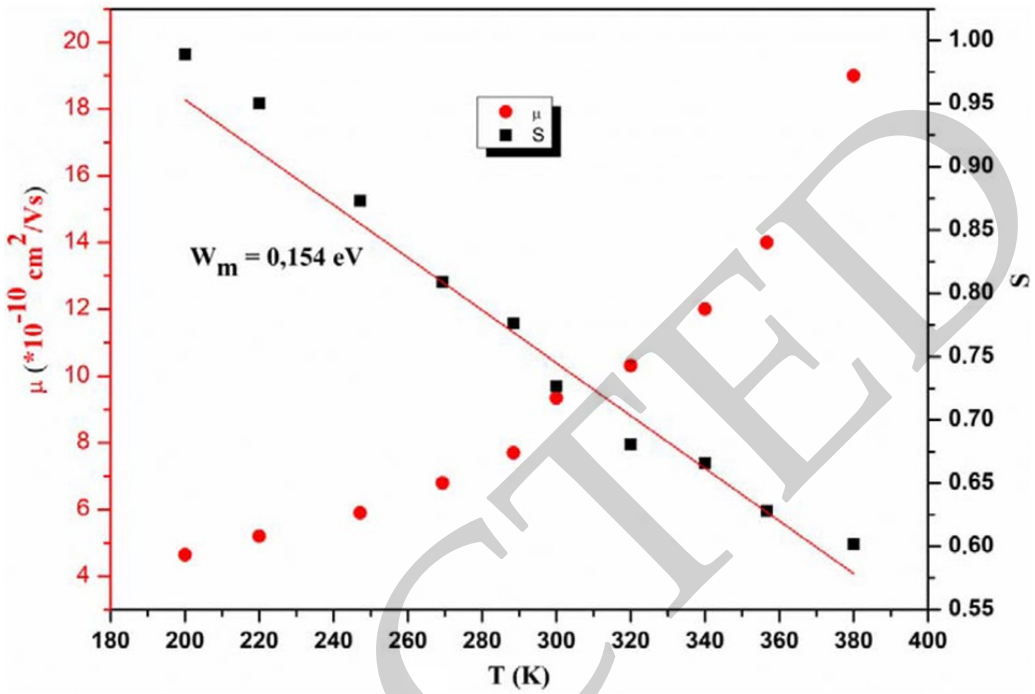


Figure 7. Temperature dependences of the charge carrier mobilities and the exponent s of $LaPbFeTiO_6$. Reprinted with permission from Nassar, K. I. et al. (2021). Applied Physics A: Materials Science & Processing [116]. Copyright © 2021 The Author(s), under exclusive license to Springer-Verlag GmbH, DE, part of Springer Nature.

Indeed, Hasan, Z., Rahman, M.A., Das, D.K. et al. [121] conducted a comprehensive first-principles investigation into the structural, electronic, optical, and mechanical properties of the pure $BaTiO_3$ and Ca-doped $BaTiO_3$ ($Ba_{1-x}Ca_xTiO_3$ with x = 0.125, 0.25, 0.375, 0.500, 0.625) perovskites, aiming to evaluate their potential for optoelectronic, photorefractive, and photovoltaic applications. Utilizing density-functional-theory calculations, the study revealed significant modifications in the properties of $BaTiO_3$ upon Ca doping. The geometrically optimized structures showed a phase transition from cubic to another crystal phase at a doping level of x = 0.25. The electronic band structure analysis indicated a change from an indirect to a direct band gap upon Ca doping, with a shift in the conduction band toward higher energy levels. The bandgap for pure $BaTiO_3$ was found to be 1.729 eV, which increased slightly with Ca doping, reaching 1.749 eV at x = 0.125 and 1.775 eV at x = 0.25, demonstrating a direct band gap at these doping levels. This direct band gap characteristic is crucial for optoelectronic and photovoltaic applications, as it enhances the material's efficiency in light absorption and emission processes [122–125]. The optical properties, including absorption, reflectivity, refractive index, extinction coefficient, conductivity, dielectric function, and loss function, were extensively studied over an energy range from 0 to 30 eV. The results highlighted a prominent absorption peak and significant optical activity in the UV light energy region, suggesting that Ca-doped $BaTiO_3$ is highly suitable for UV photo detectors and other optoelectronic devices. The mechanical properties were also analyzed, showing increased Debye temperatures with higher Ca doping levels, indicating enhanced thermal stability. The elastic constants confirmed the mechanical stability and the presence of covalent bonds in the compounds. Overall, the modification of $BaTiO_3$ by Ca doping significantly improved its structural, electronic, and optical properties, making it a multifunctional material with potential applications in vari-

RETRACTED

ous advanced technologies. The study provides a solid foundation for further experimental and theoretical research to optimize and utilize Ca-doped $BaTiO_3$ in practical applications. Extra, Md. Azizur Rahman, and their team [126] conducted an extensive study on the impact of A-cations (Ba, Sr, and Ca) on the structural, electronic, optical, mechanical, and solar cell performance of novel A_3NCl_3 perovskites using DFT and SCAPS-1D (version 3.3.10) simulation software. This research aimed to investigate lead-free halide perovskites, known for their excellent optical absorption, tunable band gap, and high carrier mobility. The study revealed that these perovskites exhibit a semiconducting nature with a direct band gap and mechanical stability, confirmed by phonon studies. The direct band gap values for Ba_3NCl_3, Sr_3NCl_3, and Ca_3NCl_3 were found to be 0.58(1.20), 1.258(1.75), and 1.683(2.30) eV, respectively, using PBE(HSE) functionals, indicating a decrease in bandgap as the A-cation changed from Ba to Sr to Ca. This trend is attributed to the increase in the cation radius, which weakens electrostatic interactions between the cations and Cl atoms, reducing the energy needed for electron transition from the valence band to the conduction band. The solar cell performance analysis, using the structure $Al/FTO/SnS_2/A_3NCl_3/Au$, showed that Ba_3NCl_3-based cells achieved the highest power conversion efficiency (PCE) of 28.81%, with a JSC of 38.26 mA/cm^2, FF of 79.91%, and VOC of 0.94 V. In contrast, cells with Sr_3NCl_3 and Ca_3NCl_3 had PCEs of 18.11% and 8.54%, respectively. The electronic band structures indicated a transition from an indirect to a direct bandgap, essential for photovoltaic and optoelectronic applications [126]. The study also examined the partial density of states, revealing hybridization of the Ca, Sr, Ba, and N states with Cl, indicating ionic bonding between these elements. The valence band maximum (VBM) was mainly influenced by the Cl-2p orbital, while the conduction band minimum (CBM) was determined by the N-2p and A (Ca, Sr, Ba)-p orbitals. This comprehensive analysis provides valuable insights into the experimental development of efficient A_3NCl_3-based perovskite solar cells (Figure 8).

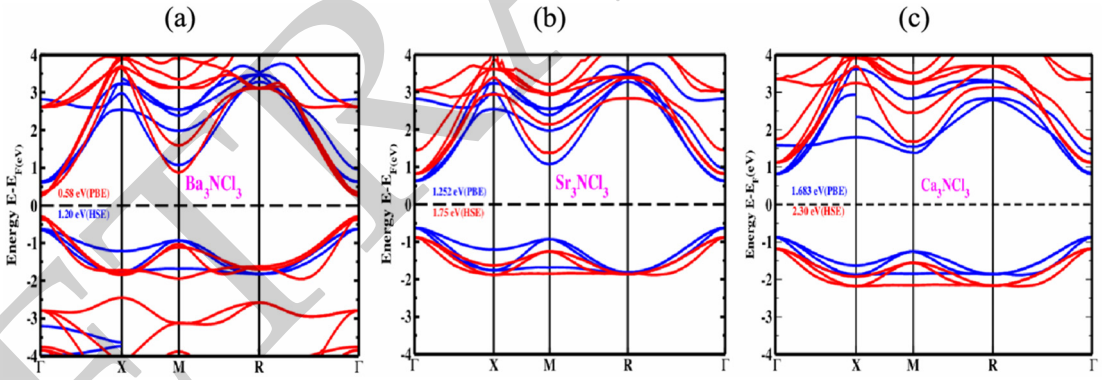


Figure 8. (**a**) Ba_3NCl_3, (**b**) Sr_3NCl_3, and (**c**) Ca_3NCl_3 electronic band structures using the PBE and HSE functions of inorganic novel A_3NCl_3 perovskites. Reprinted with permission from Rahman, M. A. et al. (2024). Energyfuels.3c03175 [126]. Copyright © 2024 American Chemical Society.

Nassar, K.I., Benamara, M., Kechiche, L., and their colleagues [127] studied the structural, microstructural, and electrical properties of bismuth and niobium-doped $LaNiO_3$ perovskite synthesized via the sol-gel technique for potential electronic device applications. The X-ray diffraction analysis with Rietveld refinement indicated a monoclinic phase with a $P_{21/n}$ space group at room temperature. Scanning electron microscopy revealed closely packed grains with high density and minimal porosity. The dielectric relaxation phenomenon analyzed using the Cole-Cole model and the complex impedance data were modeled with an equivalent circuit comprising a resistance and a constant phase element [128]. The frequency-dependent conductivity followed Jonscher's power law, while an Arrhenius-type conduction mechanism with an activation energy of 0.168 eV was iden-

RETRACTED

tified. Notably, the electrical properties remained stable across different temperatures, highlighting the material's potential for thermally stable capacitor applications. The ac conductivity study showed two plateaus in the spectra, indicating the presence of two distinct processes contributing to the bulk conduction behavior, with one relaxing in the high-frequency region and the other appearing as a plateau at high frequencies (Figure 9).

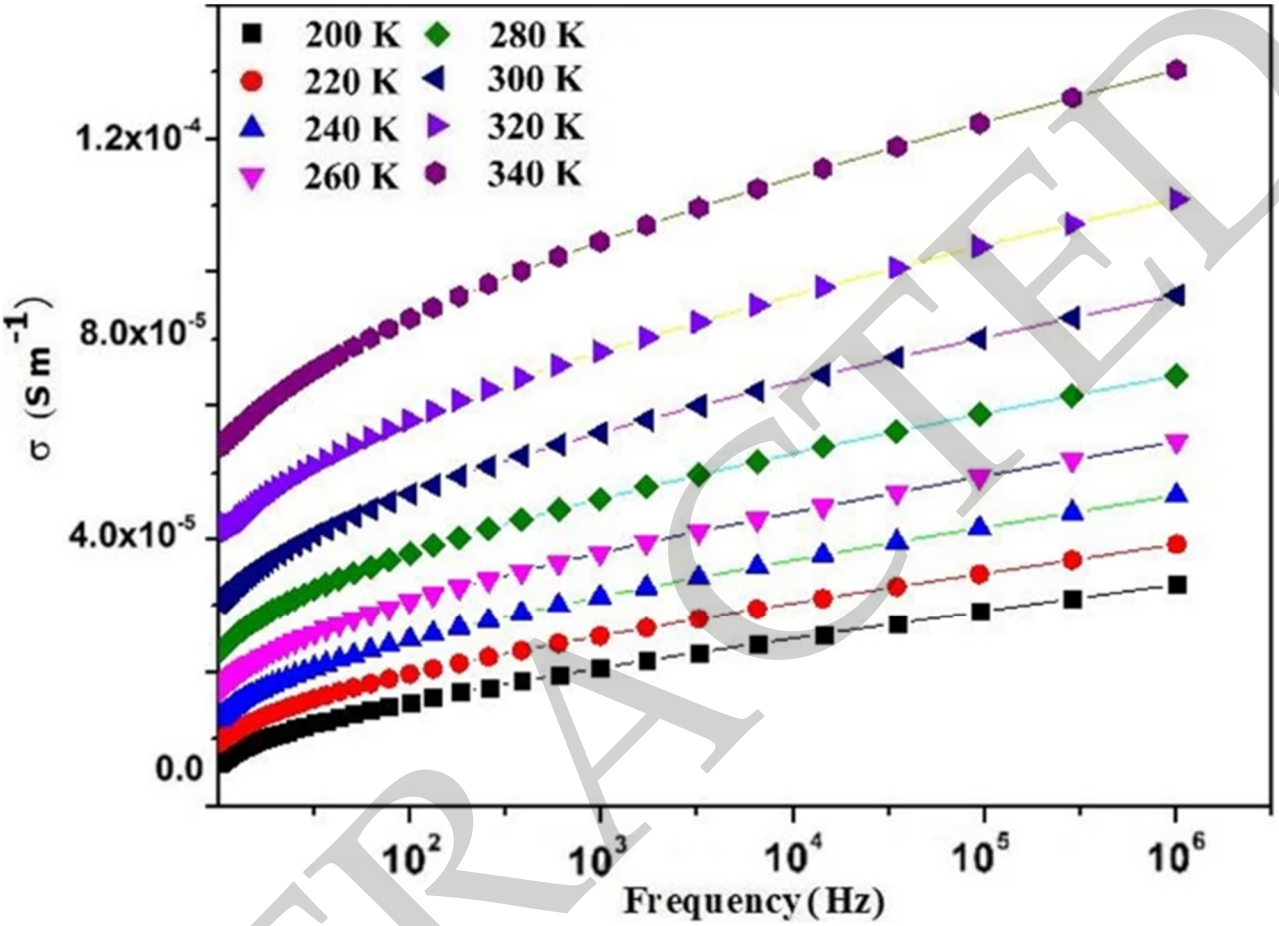


Figure 9. Variation in the conductivity σ_{AC} as a function of temperature and frequency. Reprinted with permission from Nassar, K. I. et al. (2024). Indian Journal of Physics [127]. Copyright © 2024 Indian Association for the Cultivation of Science, published by Springer Nature.

3.2. Dielectric Properties

The dielectric properties of perovskite materials are equally significant, particularly for their applications in capacitors, tunable dielectrics, and memory devices. Many perovskite compounds exhibit high dielectric constants combined with low dielectric losses, making them ideal candidates for advanced electronic components. The frequency-dependent behavior of dielectrics in perovskites, including dielectric relaxation and polarization mechanisms, plays a critical role in optimizing their performance across various applications. In their study, Iben Nassar, K., et al. [129] explored the dielectric properties of the polycrystalline sample $LaBaFe_{1.2}Mn_{0.8}O_6$ synthesized via the sol-gel method. X-ray diffraction confirmed the sample's single-phase formation in a rhombohedral crystal system with the RC space group. Detailed dielectric and impedance spectroscopy analyses over various temperatures revealed a relaxation phenomenon. The real part of the dielectric permittivity (ε') was found to increase with temperature and decrease with frequency. A notable shift in the maximum permittivity curves was observed as the temperature rose from 300 K to 620 K, indicating a dielectric relaxor behavior. The permittivity increased up to a transition temperature (T_d) of 425 K, beyond which it decreased, suggesting a metal-semiconductor

RETRACTED

transition. Additionally, the analysis of dielectric loss showed almost negligible dissipation at low temperatures, which increased significantly around 400 K and then decreased with higher frequencies at elevated temperatures, consistent with the Debye model (Figure 10). This behavior suggests that charge carriers are unable to follow the applied electric field at high frequencies, leading to reduced dielectric dissipation in this range. These findings underscore the material's potential for applications requiring high permittivity and low dielectric loss such as capacitors.

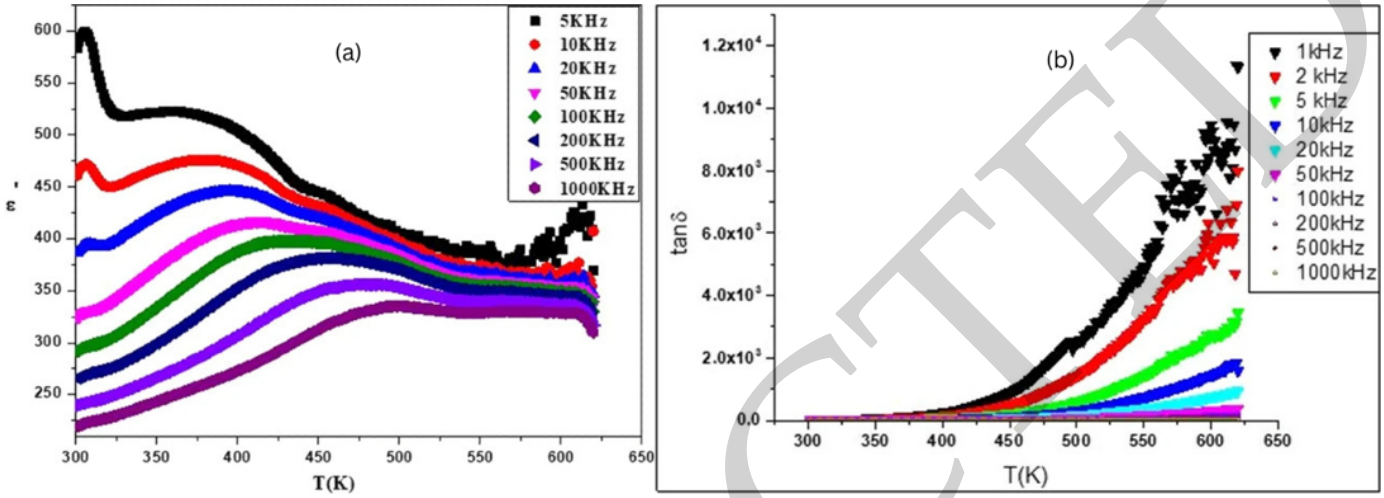


Figure 10. Temperature variation in the real part of permittivity (ε') at several frequencies (**a**) and the temperature variation in the loss tangent ($\tan\alpha$) at several frequencies of the sample (**b**). Reprinted with permission from Nassar, K. I. et al. [129]. Copyright © 2022 Indian Association for the Cultivation of Science, published by Springer Nature.

The study by Tayari et al. [130] delved into the dielectric and electrical conductivity properties of the $Ba_{0.75}Ni_{0.25}Tc_{0.88}Mn_{0.12}O_3$ (BNTMO) perovskite ceramic, synthesized using the sol-gel method. Structural analysis via X-ray diffraction confirmed a single-phase cubic structure with a Pm-3m space group, while scanning electron microscopy showed a well-defined morphology with an average particle size of 243 nm. Dielectric studies revealed that the real part of the complex permittivity (ε') increased with temperature and decreased with frequency, suggesting a dielectric polarization mechanism. This behavior, primarily due to interfacial polarization, aligns with observations in similar perovskite and metallic oxide materials. The dielectric loss also decreases with increasing frequency, attributed to relaxation time distribution and charging carrier density. These properties indicate the material's potential for energy storage applications [131]. The consistent activation energy values from various analyses further support the coherence of the charge carrier relaxation process in BNTMO, making it a viable candidate for advanced technological applications (Figure 11).

RETRACTED

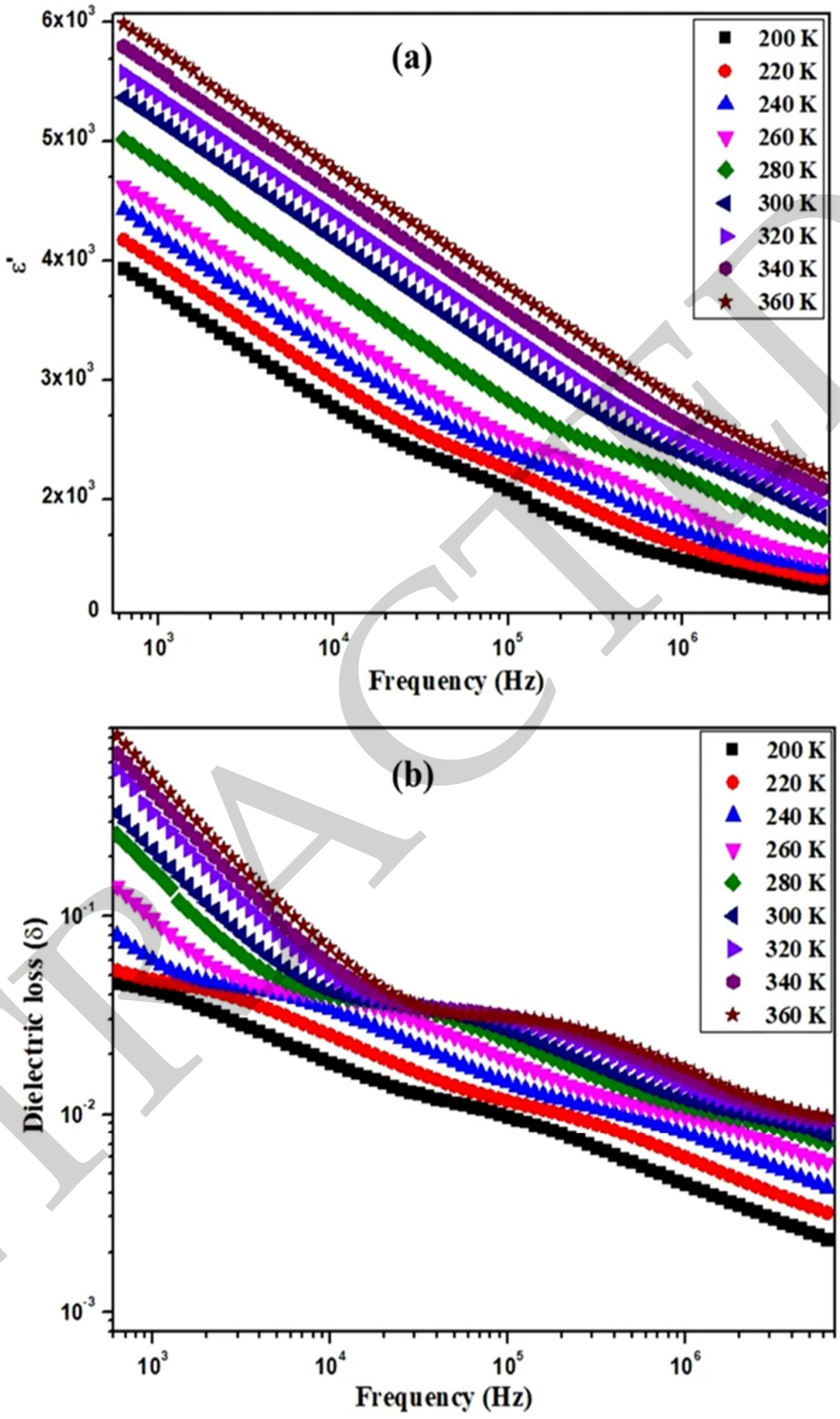


Figure 11. (**a**) Evolution of the real part of the permittivity and (**b**) the variation in dielectric loss as a function of frequency at various temperatures. Reprinted with permission from Tayari et al. (2024). Journal of Sol-Gel Science and Technology [130]. Copyright © 2024 The Author(s), published by Springer Nature.

The study by Kumar, A., Kumar, V., and Kumar, A. et al. [132] examined the dielectric and electrical properties of a $Bi_5Yb_3O_{12}$ (BYO) ceramic material synthesized via a chemical route. X-ray diffraction (XRD) and Le Bail fitting confirmed the single-phase formation of

RETRACTED

a BYO ceramic with a cubic crystal system and space group Fm-3m. X-ray photoelectron spectroscopy (XPS) verified the oxidation states of the elements, while energy-dispersive X-ray spectroscopy (EDS) determined the elemental composition. The dielectric constant of the BYO ceramic reached a peak value of 337 at 382 K and 1 kHz, and its lowest value was 238 at 523 K and 1 kHz, with a tangent loss (tan δ) of 0.2 at 293 K and 1 kHz, and 0.37 at 293 K and 1 MHz The dielectric constant (ε') and dielectric loss (tan δ) of the BYO ceramic were studied over various temperatures and frequencies, showing that the dielectric constant was higher at low frequencies due to contributions from various polarization types, such as electronic, ionic, dipolar, and interfacial, and decreased with increasing frequency, where electronic polarization dominated. Additionally, temperature influenced the dielectric constant, which initially increased but decreased beyond a certain point, reflecting the material's relaxation behavior. Factors like material thickness and moisture content also affect the dielectric constant. This behavior aligns with the Maxwell-Wagner and Koop models, describing ceramic materials as having highly conducting grains and less conducting grain boundaries. The dielectric loss decreases with increasing frequency, indicating the material's relaxation dynamics and charge carrier density contributions. The study highlights BYO ceramic's potential for technical applications, particularly in capacitors, due to its high permittivity and low dielectric loss, providing insights into its suitability for electronic devices and energy storage applications (Figure 12).

In their study, Suresh et al. [133] explored the structural, optical, and dielectric properties of nanostructured $La_{1-x}Sr_xMnO_3$ perovskites synthesized via the combustion method using citric acid as fuel. X-ray diffraction (XRD) confirmed the formation of the desired compositions, revealing that increasing the Sr doping concentration reduced the crystallite size from 30 nm to 14 nm. Scanning electron microscopy (SEM) displayed a spongy, porous structure in the samples. Optical analysis showed good absorbance in the UV and higher wavelength regions, with the optical bandgap energy increasing. In their study, Jabarov et al. investigated the dielectric and electrical properties of $La_{0.5}Ba_{0.5}MnO_3$ and $La_{0.97}Ba_{0.03}MnO_3$ perovskites over a temperature range of 25–225 °C and a frequency range of 20–10^6 Hz. Their analysis revealed that the electrical conductivity of these compounds increased with temperature and frequency, and a semiconductor-metal phase transition occurred at around 140 °C. The dielectric constant and losses were characterized, showing a stable real part of the dielectric constant under varying temperature and frequency, while the imaginary part of the dielectric constant decreased with frequency. For $La_{0.5}Ba_{0.5}MnO_3$, the imaginary part stabilized after approximately 5×10^3 Hz, and significant dielectric losses were noted at lower frequencies due to the charge carrier dynamics. The temperature-dependent behavior of the imaginary part of the dielectric constant indicated the presence of impurities or radicals, influencing its increase below 90 °C and resonant interactions between 90 and 160 °C. In contrast, $La_{0.97}Ba_{0.03}MnO_3$ showed a clear increase in dielectric constant up to 140 °C, followed by a decrease, indicative of the phase transition. The findings underscore the significance of these perovskites in applications requiring controlled dielectric and conductive properties, highlighting their potential in electronic and catalytic processes. From 1.4 eV to 2.5 eV, as the Sr doping concentration increased, the dielectric analysis highlighted that $La_{0.3}Sr_{0.7}MnO_3$ exhibited a high dielectric constant at ambient temperature and low frequencies, attributed to interfacial dislocations, charge defects, oxygen vacancies, and grain boundary effects as explained by the Maxwell-Wagner model (Figure 13). The dielectric constant decreased with increasing frequency but increased with higher Sr doping concentrations, making these materials suitable for supercapacitor applications. The study also noted that ac conductivity followed Johnscher's universal power law at high frequencies, with electrode polarization effects evident from the log σ log f plot. The dielectric loss tangent (tan δ) decreased with increasing frequency, indicating

RETRACTED

higher resistivity at the grain boundaries compared with the grains. The behavior of tan δ, which decreased with increased doping, suggests its suitability for high-frequency device applications. Moreover, in their study, Jabarov et al. [134] investigated the dielectric and electrical properties of $La_{0.5}Ba_{0.5}MnO_3$ and $La_{0.97}Ba_{0.03}MnO_3$ perovskites over a temperature range of 25–225 °C and a frequency range of 20–106 Hz. Their analysis revealed that the electrical conductivity of these compounds increased with temperature and frequency, and a semiconductor-metal phase transition occurred at around 140 °C. The dielectric constant and losses were characterized, showing a stable real part of the dielectric constant under varying temperature and frequency, while the imaginary part of the dielectric constant decreased with frequency. For $La_{0.5}Ba_{0.5}MnO_3$, the imaginary part stabilized after approximately 5×10^3 Hz, and significant dielectric losses were noted at lower frequencies due to the charge carrier dynamics. The temperature-dependent behavior of the imaginary part of the dielectric constant indicated the presence of impurities or radicals, influencing its increase below 90 °C and resonant interactions between 90 and 160 °C. In contrast, $La_{0.97}Ba_{0.03}MnO_3$ showed a clear increase in dielectric constant up to 140 °C, followed by a decrease, indicative of the phase transition. The findings underscore the significance of these perovskites in applications requiring controlled dielectric and conductive properties, highlighting their potential in electronic and catalytic processes.

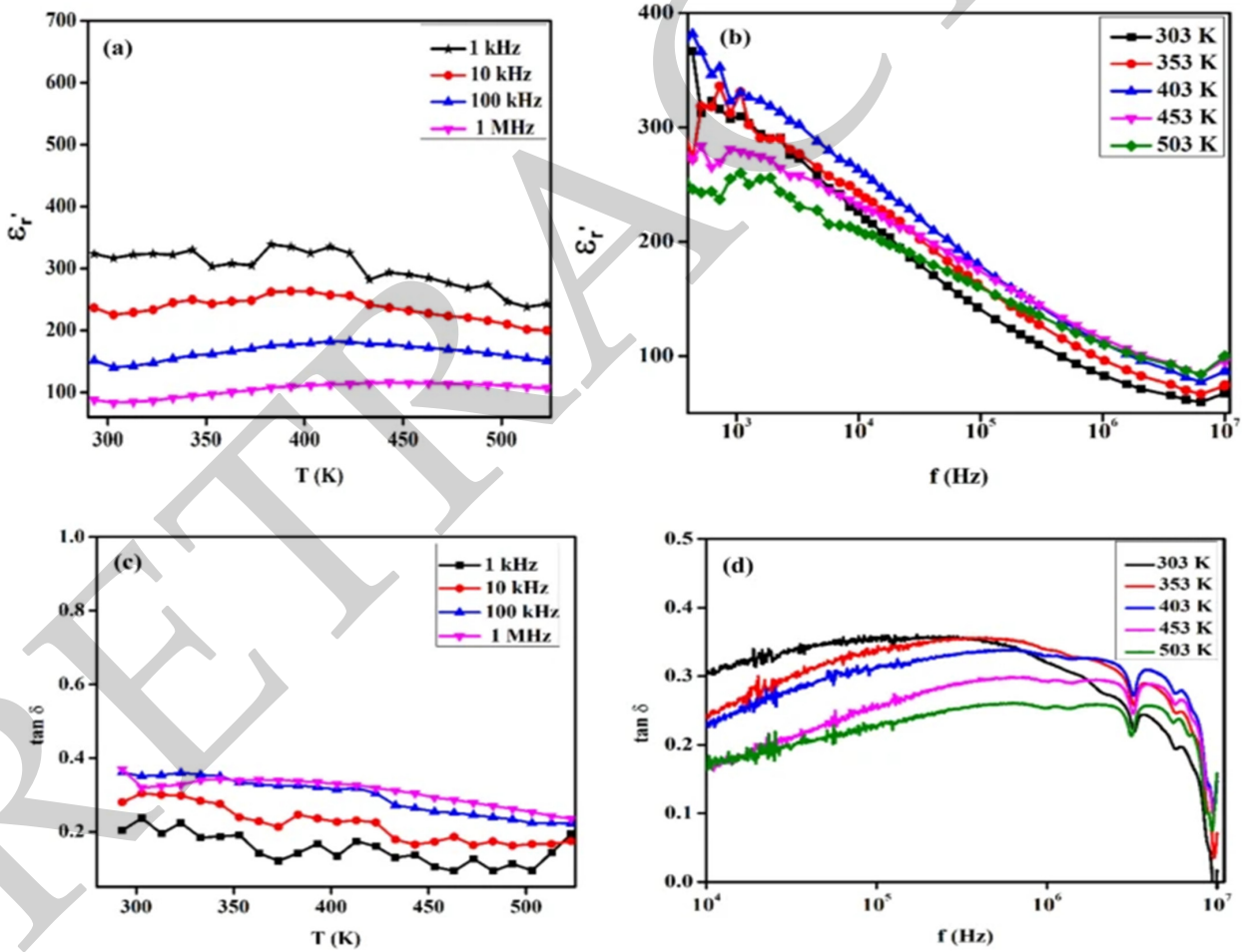


Figure 12. (**a**,**b**) Temperature and frequency dependent variation in dielectric constant (ε_r) and (**c**,**d**) temperature and frequency-dependent variation in tangent loss (tan δ) of BYO sintered at 1123 K for a duration of 8 h. Reprinted with permission from Kumar, A. et al. (2024). Journal of Materials Science: Materials in Electronics [132]. Copyright © 2024 The Author(s), under exclusive license to Springer Science Business Media, LLC, part of Springer Nature.

RETRACTED

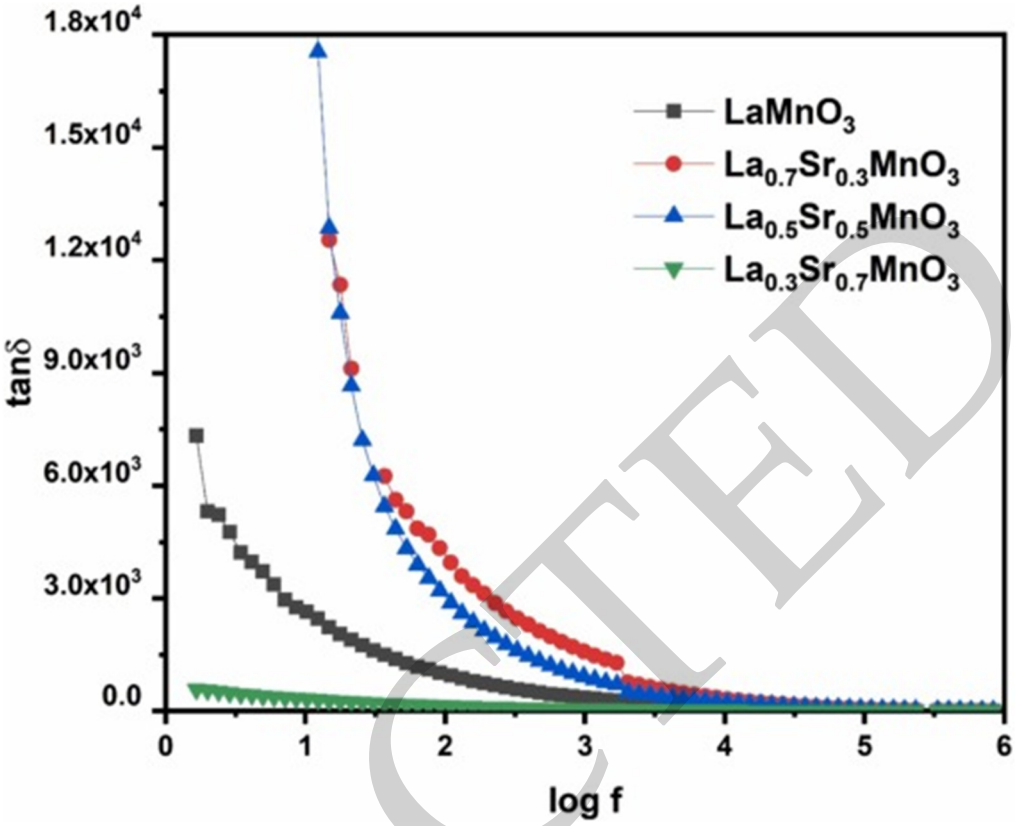


Figure 13. Variation in loss factor tan δ of $LaMnO_3$, $La_{0.7}Sr_{0.3}MnO_3$, $La_{0.5}Sr_{0.5}MnO_3$, and $La_{0.3}Sr_{0.7}MnO_3$ nanoparticles with frequency. Reprinted with permission from Suresh, S. et al. (2023). Materials Today Communications [133]. Copyright © 2023 Elsevier, published by Materials Today Communications.

Similarly, the study by Algahtani et al. [135] explored the structural, optical, and microwave dielectric properties of $Sr_2Fe_{1+x}Nb_{1-x}O_6$ ceramics synthesized via a solid-state route. Their investigation employed X-ray powder diffraction (XRD), scanning electron microscopy (SEM), Fourier transform infrared (FTIR) spectroscopy, impedance analysis, and photoluminescence (PL) spectroscopy. XRD analysis confirmed a single-phase tetragonal structure with space group I4/m across the $Sr_2Fe_{1+x}Nb_{1-x}O_6$ composition range of $0.015 \leq x \leq 0.030$. The findings indicated enhanced structure stability with increasing x. Impedance analysis revealed that increasing frequency enhanced carrier hopping and mobility, impacting conductivity. The dielectric constant showed variations with the frequency and relative densities, indicating a rise with increasing density but was affected by the impurity phases at microscopic levels. Dielectric loss, decreased with increasing frequency, was attributed to the reduced power loss from current leakage in the capacitor configuration. PL analysis highlighted an excitation energy suitable for green light lasers. Overall, the research underscores the potential of $Sr_2Fe_{1+x}Nb_{1-x}O_6$ ceramics in microwave applications, emphasizing their structural stability and favorable dielectric properties across varying compositions and densities.

4. Magnetic Properties

Perovskite materials display diverse magnetic properties, ranging from ferromagnetism and antiferromagnetism to complex magnetic ordering phenomena. These properties are essential for applications in spintronics, magnetic storage, and multifunctional materials that integrate magnetic and electronic functionalities [136]. The interplay between the structural, electronic, and magnetic characteristics of perovskites offers fertile ground

RETRACTED

for exploring new physical phenomena and developing innovative technologies. The magnetic properties of RE_2NiCrO_6 (RE = Ce, Pr, and Nd) double perovskite oxides were thoroughly investigated using experimental and theoretical approaches in the study by Irfan et al. [137]. The compounds were synthesized via the hydrothermal method, and their structural, electronic, and magnetic properties were characterized. X-ray diffraction confirmed the orthorhombic structure, while SEM images displayed well-formed particles, and EDS mapping verified the elemental composition of Ce, Pr, Nd, Ni, Cr, and O in appropriate proportions. Density functional theory calculations using the FP-LAPW method revealed the half-metallic nature of these compounds, with the spin-polarized electronic structures and density of states indicating ferromagnetic coupling between the Ni and Cr ions. The magnetic properties were further elucidated through magnetization measurements at room temperature, as depicted in Figure 14a–c. The presence of hysteresis loops with residual magnetization and coercivity confirmed the ferromagnetic behavior of the RE_2NiCrO_6 compounds. According to the Goodenough-Kanamori rule, this ferromagnetic order arises from the virtual electron transfer between transition metal ions. The experimentally calculated values of magnetic saturation (Ms), coercivity (Hc), and retentivity (Mr) had Ms values of 5.96 emu/g, 7.93 emu/g, and 9.95 emu/g for the Ce, Pr, and Nd compounds, respectively. These values correlated well with the theoretical predictions and highlight the potential of RE_2NiCrO_6 double perovskite oxides for applications in spintronics due to their robust ferromagnetic properties and half-metallic character [137].

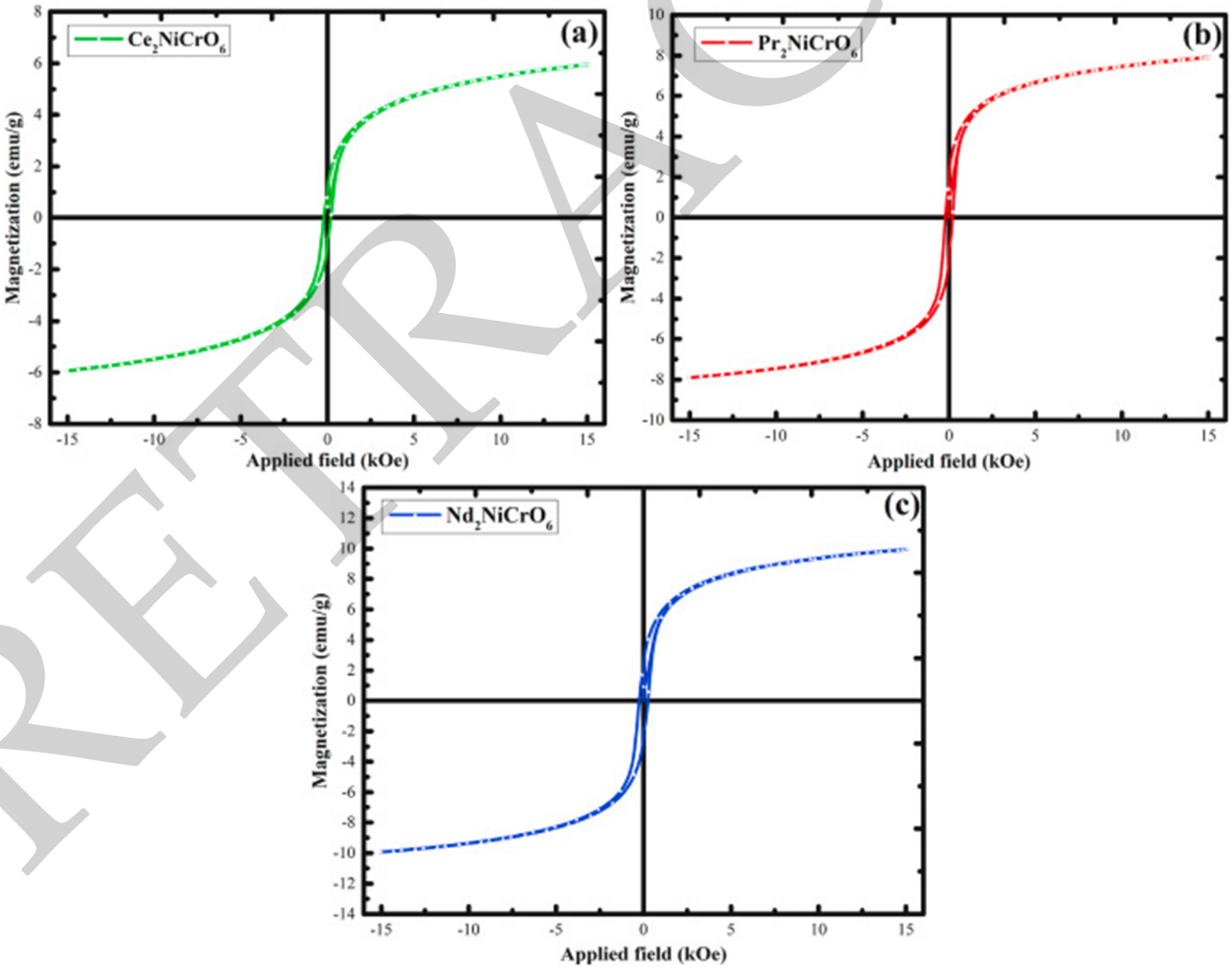


Figure 14. (**a**–**c**) Magnetization curves of (**a**) Ce_2NiCrO_6, (**b**) Pr_2NiCrO_6, and (**c**) Nd_2NiCrO_6 double perovskite oxides. Reprinted with permission from the author(s) (2023). Physica E: Low-dimensional Systems & Nanostructures [137]. Copyright © Elsevier, published by Elsevier BV.

RETRACTED

The investigations conducted by Marouane et al. [138] looked at the impact of potassium (K) substitution at the A-site on the structural, magnetic, and magnetocaloric properties of brownmillerite oxides $La_{1-x}K_xSrMn_2O_{5+\delta}$ ($0.1 \leq x \leq 0.3$). Synthesized via solid-state reaction at high temperatures, the compounds were found to crystallize in the orthorhombic system with a Pnma space group, as revealed by structural analysis. Magnetic measurements, including Arrott's analysis, identified a second-order ferromagnetic phase transition in all samples, where the Curie temperature (T_C) decreased with increasing potassium content. Specifically, T_C values were observed at 357 K, 354 K, and 350 K for x = 0.1, 0.2, and 0.3, respectively. This reduction in T_C with higher K substitution can be attributed to changes in the Mn^{3+} and K^{3+} concentrations, influencing super exchange interactions. The magnetocaloric effect, quantified by the isothermal magnetic entropy change $|\Delta SM|$, indicated values of 1.2 J kg^{-1} K^{-1}, 1.08 J kg^{-1} K^{-1}, and 0.8 J kg^{-1} K^{-1} for x = 0.1, 0.2, and 0.3, respectively. Overall, these findings underscore the tunability of magnetic and magnetocaloric properties in $La_{1-x}K_xSrMn_2O_{5+\delta}$ through controlled potassium substitution, highlighting their potential for magnetic refrigeration applications (Figure 15). Similarly, S. Belhamra et al. [84] studied the structural, electronic, magnetic properties, and magnetocaloric effects of $LaRO_3$ (R = Mn, Cr, Fe) perovskite oxides using first-principles calculations and Monte Carlo simulations. Their research revealed that these materials exhibited intrinsic weak ferromagnetism at room temperature, attributed to the unique structural arrangements of transition metal ions and oxygen octahedra. The temperature-dependent magnetization curves indicated broad peaks in magnetic entropy change (ΔS) around room temperature: 137 K for $LaCrO_3$, 350 K for $LaMnO_3$, and 785 K for LaFeO3. Furthermore, the comparative analysis of magnetic hysteresis loops showed distinctive coercive fields (hC) and remanent magnetizations (Mr) among the compounds, with $LaCrO_3$ displaying superparamagnetic behavior and $LaMnO_3$ and $LaFeO_3$ exhibiting typical ferromagnetic characteristics. These findings underscore the potential of $LaRO_3$ perovskites as efficient materials for magnetic refrigeration applications due to their competitive relative cooling powers.

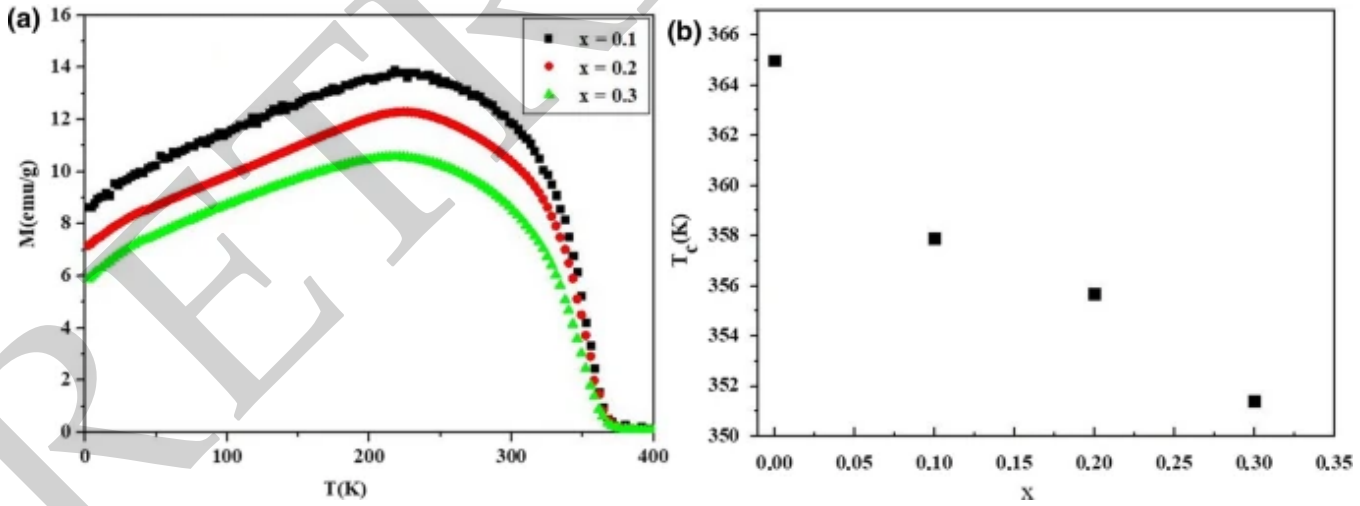


Figure 15. (**a**) Temperature dependence of the magnetization at H = 0.005, TH = 0.005 T for $La_{1-x}K_xSrMn_2O_{5+}\delta$ and (**b**) Curie temperature dependence as a function of xx for $La_{1-x}K_xSrMn_2O_{5+}\delta$ with x = 0.1, 0.2, 0.3, x = 0.1, 0.2, 0.3. Reprinted with permission from Mohamed, M. et al. (2022). Indian Journal of Physics [138]. Copyright © 2022 Indian Association for the Cultivation of Science, published by Springer Nature.

The study by Quanli Hu et al. [139] investigated the electrochemical and magnetic properties of perovskite type rare earth manganite nanofibers, specifically $LaMnO_3$,

REPRINTED

$NdMnO_3$, and $SmMnO_3$, fabricated via electrospinning. The structural characterization revealed a rhombohedral structure for $LaMnO_3$ and orthorhombic structures for $NdMnO_3$, $SmMnO_3$, and $EuMnO_3$ NFs. The $RMnO_3$ were examined for their electrochemical behavior as supercapacitor electrodes, demonstrating promising specific capacitances and cycle stability, despite some needing improvement. Regarding magnetic properties, the NFs exhibited paramagnetic behavior at room temperature. At low temperatures, $LaMnO_3$ and $NdMnO_3$ NFs displayed a transition to ferromagnetic states, while $SmMnO_3$ and $EuMnO_3$ NFs exhibited transitions to antiferromagnetic states. Magnetic hysteresis loops at 10 K indicated ferromagnetic behavior for $LaMnO_3$ and $NdMnO_3$ NFs, with saturation magnetizations of 44.58 and 69.81 emu/g, respectively. In contrast, $SmMnO_3$ and $EuMnO_3$ NFs showed weak ferromagnetic components within antiferromagnetic phases. The coercivity of $EuMnO_3$ NFs was notably high at 3915 Oe. These findings underscore the multifaceted applications of $RMnO_3$ NFs in both the electrochemical and magnetic fields, warranting further exploration into enhancing their performance for advanced energy storage and magnetic device applications. In the same context, in their study, Idrissi et al. [140] explored the structural, electronic, and magnetic properties of the rare earth-based solar perovskites $GdAlO_3$, $DyAlO_3$, and $HoAlO_3$ by using density functional theory implemented in Quantum Espresso. The research focused on optimizing the unit cells of these materials to assess their stability and ferromagnetic behavior. They found that cubic $HoAlO_3$ exhibited the highest stability among the studied compounds, with $DyAlO_3$ being more stable than $GdAlO_3$ within this structure. Electronic structure analysis via band structure and density of states revealed that $GdAlO_3$ behaved as a semiconductor, while $DyAlO_3$ and $HoAlO_3$ displayed a half-metallic ferromagnetic character. The spin-polarized magnetic moments calculated for these materials indicate a clear ferromagnetic nature, with magnetic moments of 7.02 μ_B for $GdAlO_3$, 5.00 μ_B for $DyAlO_3$, and 4.00 μ_B for $HoAlO_3$. These findings suggest that these perovskite materials hold promise for applications in spintronics, optoelectronics, and potentially as photovoltaic materials. The study underscores their potential in advancing next-generation electronic and energy technologies. Extra, Yaiza Asensio et al. [141] discussed the magnetic properties of layered hybrid organic-inorganic metal-halide perovskites (HOIPs), specifically focusing on how different compositions and perovskite phases influenced these properties. It highlighted the role of transition metals in the crystal structure as crucial for inducing magnetic behavior. The study compared various systems with Cu^{2+} ions, detailing their temperature-dependent magnetization (M(T)) curves and magnetic hysteresis loops (M(H)s). For example, in PEA_2CuCl_4 RP crystals, long-range ferromagnetic (FM) order is observed with a Curie temperature (T_C) around 12 K, attributed to intralayer Cu–Cu spin interactions and weak interlayer interactions. Conversely, EA_2CuCl_4 RP crystals exhibited FM behavior at $T_C \approx 11$ K, with stronger interlayer antiferromagnetic (AFM) contributions due to a shorter interlayer distance. The text further explored DJ phase HOIPs like $PEAACuCl_4$ and $EDACuCl_4$, noting shifts in TC and magnetization saturation fields (HS) due to changes in crystal structure and interlayer distances. In Mn^{2+} HOIPs, such as PEA_2MnCl_4 RP crystals, the magnetic behavior was dominated by intralayer AFM interactions with a weak FM component arising from spin-canting effects due to crystal structure distortions. Overall, the discussion underscores how structural variations in HOIPs influence their magnetic properties, impacting their potential applications in spintronics and related fields. Furthermore, Yaiza Asensio et al. [142] investigated the impact of La doping on the structural and magnetic properties of $Ca_{1-x}La_xFe_{0.5}Mn_{0.5}O_{3-\delta}$ perovskites synthesized via the solid-state method.

Using X-ray diffraction and magnetic measurements, they explored these materials across a doping range ($0.05 \leq x \leq 0.15$). Their structural analysis revealed that all phases crystallized in the cubic system with a Pm-3m space group. Electron density studies high-

RETRACTED

lighted the formation of partial covalent and ionic bonds involving Mn/Fe-O and Ca/La-O units, alongside an ordered arrangement of oxygen vacancies. Magnetic investigations indicated a paramagnetic to antiferromagnetic transition as the temperature decreased, with a decrease in Neel temperature (T_N) attributed to enhanced ferromagnetic interactions due to La doping. Furthermore, they observed weak ferromagnetism at room temperature, as evidenced by non-null magnetization and magnetic hysteresis loops. Below T_N, complex magnetic responses including antiferromagnetic, ferromagnetic, and ferrimagnetic ordering were observed, influenced by exchange interactions and antiphase boundaries. This study underscores the potential technological relevance of these materials, particularly their observed exchange bias effect and ambient temperature ferromagnetism (Figure 16) [143].

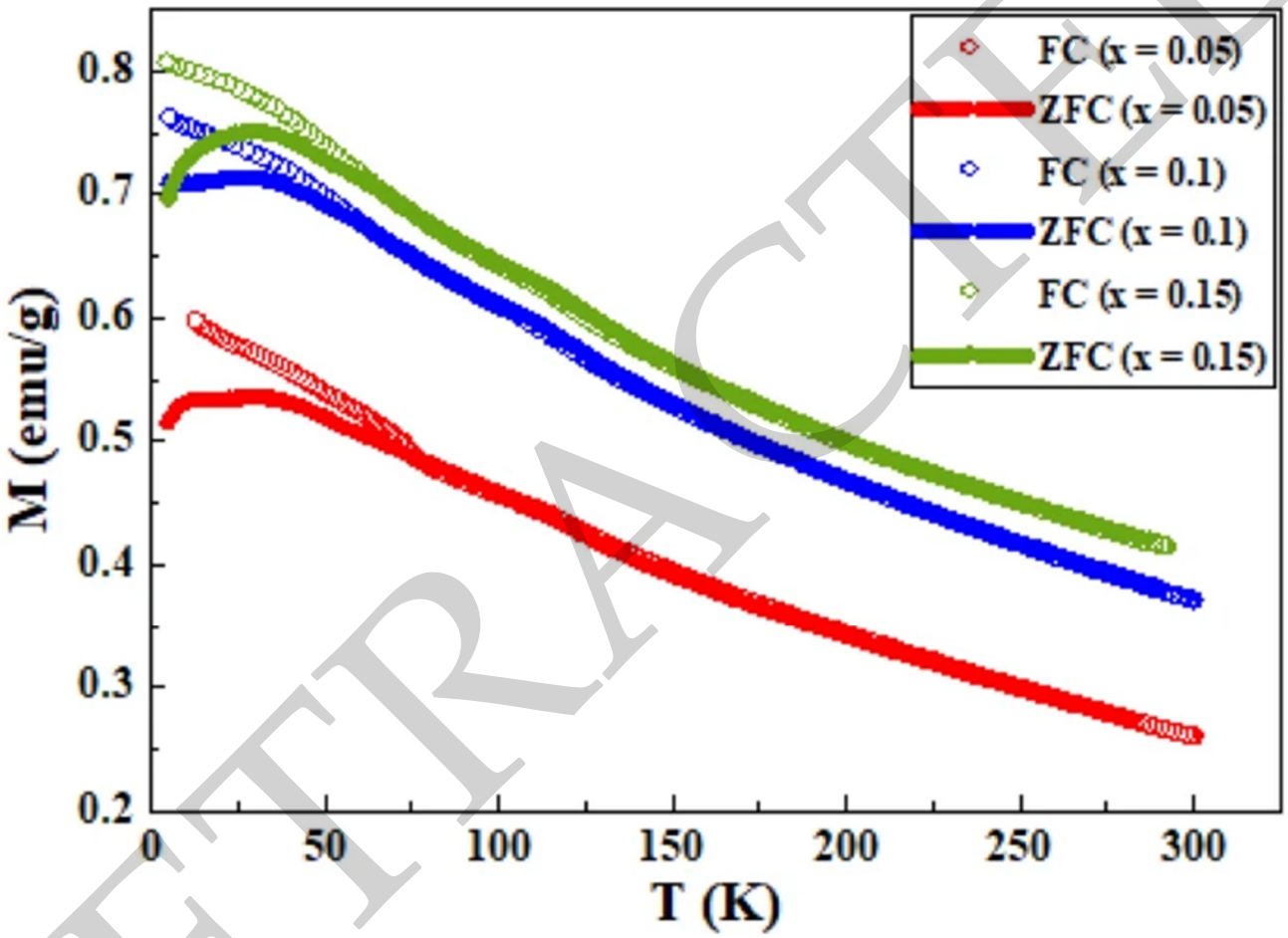


Figure 16. Thermal variation in the ZFC and FC magnetization of $Ca_{1-x}La_xFe_{0.5}Mn_{0.5}O_{3-\delta}$ ($0.05 \leq x \leq 0.15$) ceramics in an applied magnetic field of 0.2 T. Reprinted with permission from Selmi, R. et al. [143]. Copyright © 2022 The Author(s), under exclusive license to Springer-Verlag GmbH, DE, part of Springer.

In their study, Zheng et al. [144] investigated the effects of titanium (Ti) substitution on the magnetic properties and magnetocaloric effect (MCE) of Gd_2CoMnO_6 double perovskites. These materials are of interest for magnetic refrigeration due to their potential in achieving enhanced MCE at cryogenic temperatures. The researchers synthesized $Gd_2CoMn_{1-x}Ti_xO_6$ samples (x = 0–1.0) using a solid-state reaction method and characterized them for their crystal structure, surface morphology, magnetic behavior, and magnetocaloric properties.

The researchers proposed a mechanism attributing this enhanced cryogenic magnetocaloric effect to the magnetic phase transition behavior influenced by Ti substitution.

RETRACTED

They conducted detailed magnetic field dependence studies (M vs. H) at 5 K and 50 K to analyze the magnetization behavior. At 5 K, the M vs. H curves displayed antiferromagnetic characteristics with negligible hysteresis, indicating the potential for excellent MCE performance at low temperatures [145–147]. In contrast, at 50 K, hysteresis behaviors were observed in the M vs. H curves, reflecting weakened ferromagnetic interactions with increasing Ti content. Overall, the comprehensive investigation by Zheng et al. underscores the effectiveness of Ti substitution in enhancing the magnetocaloric properties of Gd_2CoMnO_6 perovskites, making them promising candidates for advanced magnetic refrigeration technologies.

Furthermore, in their study on $La_{1-x}R_xFeO_3$ (R = Co, Al, Nd, Sm) [148] perovskite nanomaterials synthesized via the sol-gel method, Fang Yang et al. investigated the structural and magnetic properties across different doping compositions. They employed X-ray diffraction, thermogravimetric analysis-differential thermal analysis (TG-DTA), and a vibrating sample magnetometer (VSM) to characterize these materials. For $La_{1-x}CoFeO_3$, increasing the Co^{2+} content led to a shift in diffraction peaks toward larger angles, accompanied by an increase in grain size (50.7 nm to 133.5 nm) and enhanced magnetic loop area and magnetization. Conversely, doping with Al^{3+} in $La_{1-x}Al_xFeO_3$ resulted in a reduction in grain size (down to 17.9 nm) and an increase in magnetization, although the material exhibited weakened ferromagnetic properties possibly due to altered sintering conditions. Nd^{3+} and Sm^{3+} doping improved magnetization and particle refinement, with $La_{0.85}Co_{0.15}FeO_3$ showing increased magnetization with longer calcination times. The magnetic hysteresis loops confirmed saturation magnetization at 8000 Oe for the $La_{1-x}Co_xFeO_3$ samples, reinforcing the influence of doping on magnetic behavior. These findings underscore the role of controlled doping in tailoring structural and magnetic properties of perovskite nanomaterials, crucial for optimizing their performance in various applications. Significant advancements have been made in the study of magnetic properties, leading to novel insights and potential applications. Veliu et al. [149] elucidated the intricate dynamics of antiferromagnetically coupled sublattices, revealing the occurrence of two-step spin-crossover transitions.

These findings underscore the complex equilibrium and nonequilibrium behaviors inherent in such systems, thereby enhancing our understanding of magnetic phase transitions and their applications in advanced magnetic materials. Meanwhile, Thach et al. [150] conducted a comparative analysis of domain wall motion driven by spin transfer torque (STT) and spin orbit torque (SOT) in ferrimagnetic GdFeCo wires. Their research highlights the distinct mechanisms and efficiencies of STT and SOT in manipulating magnetic domains, which is crucial for the development of next-generation spintronic devices.

In their study, Su et al. [151] investigated the electrochemical and magnetic properties of $PrFeO_3$ and $EuFeO_3$ nanofibers synthesized using a straightforward fabrication method. Both types of nanofibers exhibited uniform, continuous morphologies with orthorhombic perovskite structures and average diameters of 233 nm for $PrFeO_3$ and 176 nm for $EuFeO_3$.

The electrochemical performance, characterized by specific capacitances of 123 F g^{-1} and 143 F g^{-1} at 1 A g^{-1} for $PrFeO_3$ and $EuFeO_3$, respectively, was attributed to the redox reactions involving Fe^{3+}/Fe^{4+} and $Fe(CN)_{63}/Fe(CN)_{64}$. Magnetic measurements revealed distinct behaviors: $PrFeO_3$ nanofibers demonstrated stable antiferromagnetic properties without spin-glass behavior or magnetic phase transitions, whereas $EuFeO_3$ nanofibers exhibited inhomogeneous magnetic properties with a transition from paramagnetic to ferromagnetic states at low temperatures, confirmed by a bifurcation in the ZFC and FC magnetization curves below 10 K. Both materials showed strong local short-range ferromagnetic interactions at 5 K, transitioning to paramagnetic states at 300 K. These findings suggest potential applications of these nanofibers in supercapacitors and con-

RETRACTED

densed matter physics, leveraging their unique electrochemical and magnetic properties. Hossain et al. [152] synthesized $Nd_2Ni_{1-x}Co_xMnO_{6-\delta}$ ($0.2 \leq x \leq 0.5$) perovskite oxides using the citric-nitrate method and investigated their structural, optical, and magnetic properties. X-ray powder diffraction (XRD) and Rietveld analysis revealed that the unit cell parameters and volume increased with cobalt doping. Optical studies using UV-Vis spectroscopy showed an absorption peak around 330 nm, with a slight influence on the energy band gap due to Co doping. Magnetically, the partial substitution of Ni with Co at the B-site led to a decrease in Curie temperature (T_C) and increased the irreversibility between zero-field cooled (ZFC) and field-cooled (F_C) states below T_C. Magnetization studies as a function of external magnetic field at various temperatures confirmed the presence of ferromagnetic and paramagnetic phases, with saturation magnetization derived from the law of approach to saturation. At 2 K, the remanence saturation ratio increased with Co doping but decreased at higher temperatures (165 K and 200 K), and the coercivity increased monotonically with Co concentration due to magnetic domain wall pinning effects. The study suggested that Co doping increased the concentration of mixed Mn^{3+}/Mn^{4+} and Ni^{3+}/Co^{3+} ions, and the observed magnetic moments were lower than expected due to antiferromagnetic interactions and diamagnetic low-spin Co^{3+} ions. This led to magnetic frustration, aligning with the temperature-dependent ZFC and FC data, highlighting the combined magnetic effects of NdNi (Co)$O_{3-\delta}$ and $NdMnO_{3-\delta}$.

In addition, Dzara et al. [153] investigated the influence of the rare earth cation on the magnetic properties of 12R-$Ba_4M^{4+}Mn_3O_{12}$ (M = Ce, Pr) perovskites, focusing on cluster magnetism in the Mn_3O_{12} trimers and the role of the bridging MO_6 octahedron. The study confirmed the frustrated antiferromagnetic ground state of 12R-$Ba_4PrMn_3O_{12}$ below TN ≈ 7.75 K. The Pr^{4+} cation caused more complex magnetic properties than Ce^{4+}, with 12R-$Ba_4PrMn_3O_{12}$ exhibiting a sharp antiferromagnetic transition at $T_2 \approx 12.15$ K and an additional transition at $T_1 \approx 200$ K, likely related to canted antiferromagnetic order. In contrast, 12R-$Ba_4CeMn_3O_{12}$ showed no hysteresis or net moment at low temperatures. The study demonstrated that the magnetic properties of these materials could be tuned by varying the rare earth cation, highlighting the role of Pr^{4+} in introducing complex magnetic interactions and potential for material design within the hexagonal, layered perovskite family (Figure 17).

Magnetic properties play a pivotal role in perovskite materials, influencing their applications across various technological domains such as spintronics, data storage, and magnetic refrigeration [154]. Perovskite oxides, with their versatile crystal structures and tunable magnetic behaviors, have attracted significant research interest due to their potential for high-performance magnetic and electronic devices. Perovskites exhibit a rich spectrum of magnetic phenomena including ferromagnetism, antiferromagnetism, ferrimagnetism, and even complex magnetic orders such as spin glass and frustrated magnetism. For instance, the compound $LaMnO_3$ demonstrates colossal magnetoresistance due to its strong electron-lattice interactions, making it promising for next-generation memory devices. Moreover, $LaMnO_3$ is a fascinating compound within the perovskite family, known for its intricate magnetic properties and diverse applications. It crystallizes in the orthorhombic perovskite structure (space group Pbnm), where La and Mn occupy the A and B sites, respectively, and O fills the X site. The magnetic behavior of $LaMnO_3$ is primarily governed by the electronic configuration and the coupling between the magnetic moments of Mn ions. At ambient conditions, it typically exhibits antiferromagnetic ordering, where neighboring Mn spins align antiparallelly within the crystal lattice. This antiferromagnetic phase arises from the super exchange interactions mediated by oxygen ions between adjacent Mn ions, leading to a Néel temperature around 140 K.

RETRACTED

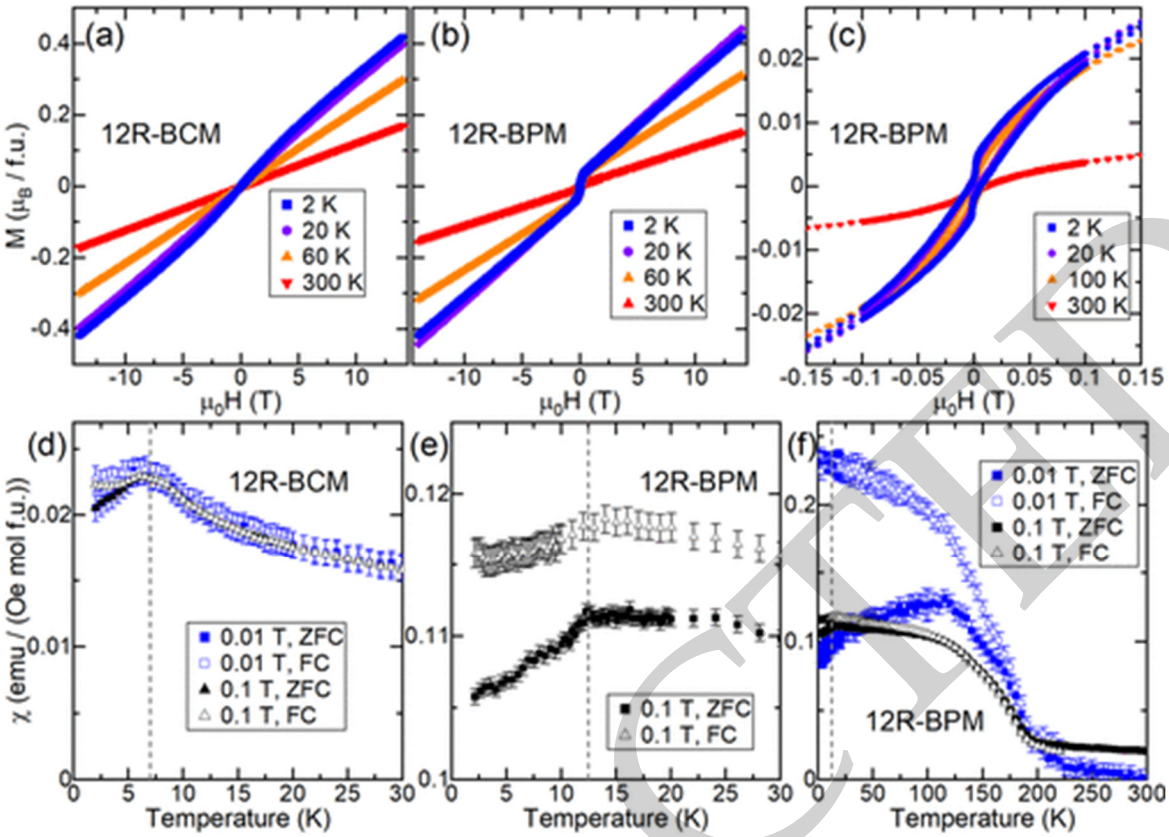


Figure 17. (**a**,**b**) Magnetization (M) as a function of the applied field for (**a**) 12R-BCM and (**b**) 12R-BPM. (**c**) Magnified low-field view of M vs. applied field for 12R-BPM. (**d**) DC susceptibility (χ) of 12R-BCM in low applied fields. (**e**,**f**) χ of 12R-BPM in low applied fields. The dashed lines denote the approximate position of each material's low-temperature transition. ZFC signifies zero-field-cooled, and FC signifies field-cooled. Reprinted with permission from Dzara, M. J. et al. Chemistry of Materials, 36(6) [153]. Copyright © 2024 American Chemical Society.

Below TN, the spins order in a manner that minimizes the magnetic energy, resulting in a unique magnetic structure that influences its physical properties. It is also known to display complex magnetic behaviors under different conditions such as the application of external fields or doping with other ions. For instance, upon doping with divalent ions like Ca^{2+}, the material can exhibit ferromagnetic or ferrimagnetic behavior, depending on the doping concentration and the nature of the substituting ions [155]. This tunability makes $LaMnO_3$ a versatile platform for studying magnetic phase transitions and for potential applications in spintronics and magnetic memory devices. On the other hand, materials like $SrFeO_{3-\delta}$ exhibit high-temperature antiferromagnetism, essential for stable magnetic data storage applications. $SrFeO_{3-\delta}$, another intriguing perovskite compound, exhibits complex magnetic properties that have made it a subject of intensive research for various technological applications. This material crystallizes in the perovskite structure, where Sr and Fe occupy the A and B sites, respectively, and O fills the X site. The magnetic behavior of $SrFeO_{3-\delta}$ is influenced by its oxygen deficiency, which can vary and affect its electronic and magnetic structure.

Perovskite-based magnetic refrigerants offer an alternative to conventional refrigerants like fluorocarbons, addressing environmental concerns while improving energy efficiency. Magnetochemistry in perovskites explores the interplay between magnetic ions, crystal structure distortions, and electronic states, which collectively dictate their magnetic properties. For example, doping $LaFeO_3$ with various transition metals alters its magnetic structure, affecting its magnetic and electrical transport properties. Understanding these

RETRACTED

relationships is crucial for tailoring perovskite materials with the desired magnetic functionalities for specific applications. Furthermore, the discovery of multiferroic perovskites, exemplified by $BiFeO_3$, where magnetic and ferroelectric orders coexist and couple, opens new avenues for multifunctional device integration [156]. Such materials exhibit promising characteristics for spin-electronics and novel sensor technologies, leveraging the coupling between magnetic and electrical properties. In the realm of entropy and magnetic perovskites, the study of magnetic entropy changes provides insights into their potential for magnetocaloric applications. Materials exhibiting large magnetic entropy changes, such as $La_{0.67}Ca_{0.33}MnO_3$, are studied for their efficiency in magnetic refrigeration cycles. This research area bridges fundamental thermodynamics with material science, aiming to optimize cooling efficiency and minimize environmental impact. Overall, the magnetic properties of perovskite materials represent a dynamic field of research with profound implications for both fundamental science and technological innovation. Continued advancements in magnetochemistry, entropy effects, and magnetic refrigeration will further expand the scope of perovskite applications in emerging technologies. The comprehensive understanding of these properties enables the design and development of advanced materials tailored for next-generation magnetic devices and sustainable cooling solutions.

5. Conclusions and Perspectives

Perovskite materials stand at the forefront of advanced material research due to their extraordinary electrical, dielectric, and magnetic properties, coupled with their structural flexibility and compositional tunability. This review has outlined the critical advancements in understanding and optimizing these properties for diverse technological applications including energy storage, spintronics, and magnetic refrigeration. Despite the immense progress achieved, several challenges remain. These include the need for improved stability under environmental stress, enhanced reproducibility in synthesis, and scalable manufacturing processes for industrial applications. Addressing these issues will be pivotal in transitioning perovskite technologies from research to commercial viability.

Future research should focus on developing novel compositions and hybrid systems that combine perovskites with other material classes to achieve multifunctionality and enhanced performance. Additionally, integrating machine learning and advanced characterization techniques could accelerate the discovery of new perovskite materials and provide deeper insights into their behavior. The field of perovskite materials research continues to expand rapidly, driven by the growing demand for high-performance, sustainable, and multifunctional materials. By addressing existing challenges and leveraging new technologies, perovskites have the potential to revolutionize a wide range of applications, paving the way for innovative solutions in energy, electronics, and beyond.

6. Challenges and Future Directions

Despite the remarkable advancements in perovskite materials, several challenges hinder their full-scale application. Stability under environmental conditions such as moisture, temperature, and radiation remain a critical issue, particularly for photovoltaics and sensors. Additionally, scalable and cost-effective synthesis methods that maintain high quality, coupled with reproducibility in material properties, are essential for industrial adoption. Many perovskite materials demonstrate optimal performance under specific conditions, such as low temperatures, limiting their practical use at ambient environments. Furthermore, the integration of perovskites into complex device architectures without compromising their functionality poses significant challenges. Addressing these issues requires innovative approaches including advanced compositional engineering to enhance stability and multifunctionality as well as the use of machine learning to accelerate material

RETRACTED

discovery and optimization. This is summarized in Table 1, which shows the challenges and strategies in perovskite device implementation. Hybrid systems that combine perovskites with polymers or nanocomposites offer potential solutions to overcome these limitations. Advanced characterization techniques are critical for understanding and fine-tuning the structural, electrical, and magnetic properties of perovskites. Moreover, focusing on eco-friendly synthesis methods and recyclable device designs aligns with the global sustainability goals. Overcoming these challenges will unlock the full potential of perovskites in transformative applications, such as renewable energy, advanced electronics, and next-generation magnetic devices, paving the way for a sustainable and technologically advanced future.

Table 1. Challenges and strategies in perovskite device implementation.

Challenge	Current Strategies	Future Directions
Stability under harsh conditions	- Protective coatings (e.g., encapsulation with polymers or inorganic layers) - Optimized synthesis methods (e.g., controlled temperature and humidity during deposition) - Use of stabilizers and additives to enhance material stability in air and moisture	- Development of more robust materials (e.g., stable perovskite variants) - Advanced encapsulation techniques (e.g., hybrid materials for better protection) - Engineering new perovskite formulations for better resistance to environmental factors
Scalability for industrial use	- Solution-processing methods (e.g., spin coating, spray coating) - Roll-to-roll printing for large-scale perovskite film production - Large-area deposition techniques for uniform films	- Improved scalability of synthesis methods (e.g., continuous processing methods) - Automation in production to reduce cost and improve efficiency - Optimization of material deposition techniques for seamless large-area integration
Efficiency limitations	- Doping (e.g., metal ion doping for conductivity improvement) - Compositional engineering (e.g., tuning the A-site or B-site cation for desired properties) - Light management techniques (e.g., photonic structures, light trapping)	- Development of new perovskite compositions with improved intrinsic properties - Hybrid perovskite materials combining organic and inorganic components for better performance - Integration with other energy conversion technologies for improved performance (e.g., tandem solar cells)
Material defects and grain boundaries	- Grain boundary engineering (e.g., post-deposition annealing, additive treatments) - Use of surfactants to reduce defects and improve crystallinity	- Creation of defect-free perovskite materials via novel synthesis methods - Development of self-healing perovskite materials to address defects in the crystal structure
Interfacial issues with electrodes	- Use of electron and hole transport layers (e.g., TiO_2, Spiro-OMeTAD) - Optimized electrode materials to reduce charge recombination	- Development of new interface engineering methods to improve charge transport across the interface - Use of transparent conductive materials for better electrode performance in devices

RETRACTED

Table 1. *Cont.*

Challenge	Current Strategies	Future Directions
Cost of materials	- Use of low-cost precursors and solution-based processing methods - Use of cheaper substrates and simplified fabrication techniques	- Research into more abundant and less expensive perovskite materials - Development of scalable fabrication techniques to lower production costs
Environmental concerns of lead-based perovskites	- Development of lead-free perovskites (e.g., tin-based perovskites, halide perovskites) - Encapsulation techniques to reduce the risk of lead leakage	- Continued research into the safe disposal or recycling of lead-based materials - Development of environmentally friendly materials and processes for perovskite devices
Long-term stability and operational lifetime	- Use of multi-layer structures to protect perovskites from degradation over time - Improvement of moisture, temperature, and UV stability through composite films	- Research on perovskite longevity, focusing on reducing degradation during operation - Integration with advanced weather-resistant coatings or coatings that repair themselves over time
Device architecture design	- Development of optimized cell architecture (e.g., monolithic, tandem solar cells) - Advanced interlayer design to facilitate charge transport	- New perovskite-based device architectures for higher efficiency and performance - Hybrid device configurations combining perovskites with other materials for energy applications (e.g., perovskite-silicon tandems)

Author Contributions: F.T. and K.I.N. conceptualized and designed the review framework. F.T. conducted the primary literature search and wrote the initial manuscript draft. S.S.T. and M.P.F.G. provided critical revisions and contributed to the refinement of the manuscript. K.I.N. supervised the project, provided expert guidance on the structure and content, and coordinated the contributions. All authors have read and agreed to the published version of the manuscript.

Funding: The authors acknowledge the support of FCT-Fundação para a Ciência e a Tecnologia, I.P., within the scope of the project's LA/P/0037/2020, UIDP/50025/2020, and UIDB/50025/2020 of the Associate Laboratory Institute of Nanostructures, Nanomodeling, and Nanofabrication-i3N.

Data Availability Statement: Data sharing is not applicable to this article as no datasets were generated or analyzed during the current study.

Acknowledgments: The authors acknowledge the support of FCT-Fundação para a Ciência e a Tecnologia, I.P., within the scope of the project's LA/P/0037/2020, UIDP/50025/2020, and UIDB/50025/2020 of the Associate Laboratory Institute of Nanostructures, Nanomodeling, and Nanofabrication-i3N.

Conflicts of Interest: The authors declare no conflicts of interest.

RETRACTED

References

1. Labhasetwar, N.; Saravanan, G.; Megarajan, S.K.; Manwar, N.; Khobragade, R.; Doggali, P.; Grasset, F. Perovskite-type catalytic materials for environmental applications. *Sci. Technol. Adv. Mater.* **2015**, *16*, 036002. [CrossRef] [PubMed]
2. Dong, H.; Zhang, C.; Liu, X.; Yao, J.; Zhao, Y.S. Materials chemistry and engineering in metal halide perovskite lasers. *Chem. Soc. Rev.* **2020**, *49*, 951–982. [CrossRef] [PubMed]

3. Liang, J.; Xu, W.; Wang, T.; Yang, Q.; Zhang, S. Implementing NAT Hole Punching with QUIC. In Proceedings of the 2024 IEEE 100th Vehicular Technology Conference (VTC2024-Fall), Washington, DC, USA, 7–10 October 2024; IEEE: Piscataway, NJ, USA, 2024.
4. Shi, X.; Ishtiaq, U.; Din, M.; Akram, M. Fractals of interpolative Kannan mappings. *Fractal Fract.* **2024**, *8*, 493. [CrossRef]
5. Zhang, X.; Chen, A.L.; Piao, X.; Yu, M.; Zhang, Y.; Zhang, L. Is AI chatbot recommendation convincing customer? An analytical response based on the elaboration likelihood model. *Acta Psychol.* **2024**, *250*, 104501. [CrossRef]
6. Shi, X.; Zhang, Y.; Pujahari, A.; Mishra, S.K. When latent features meet side information: A preference relation-based graph neural network for collaborative filtering. *Expert Syst. Appl.* **2025**, *260*, 125423. [CrossRef]
7. Xu, C.; Zhu, M.; Wang, Q.; Cui, J.; Huang, Y.; Huang, X.; Huang, J.; Gai, J.; Li, G.; Qiao, P.; et al. TROP2-directed nanobody-drug conjugate elicited potent antitumor effect in pancreatic cancer. *J. Nanobiotechnol.* **2023**, *21*, 410. [CrossRef] [PubMed]
8. Zhang, H.H.; Chao, J.B.; Wang, Y.W.; Liu, Y.; Yao, H.M.; Zhao, Z.P.; Niu, K. 5G Base Station Antenna Array with Heatsink Radome. *IEEE Trans. Antennas Propag.* **2024**, *72*, 2270–2278. [CrossRef]
9. Wang, Z.; Liao, Z.; Zhou, B.; Yu, G.; Luo, W. SwinURNet: Hybrid transformer-cnn architecture for real-time unstructured road segmentation. *IEEE Trans. Instrum. Meas.* **2024**, *73*. [CrossRef]
10. Luo, Y.X.; Dong, Y.L. Strain Measurement at up to 3000 °C Based on Ultraviolet-Digital Image Correlation. *NDT E Int.* **2024**, *146*, 103155. [CrossRef]
11. Pi, X.; Yan, D.; Xu, Y.; Pan, M.; Wang, Z.; Chang, M.; Qi, Z. TLRs signaling pathway regulation, antibacterial and apoptotic activity of largemouth bass ECSIT during Edwardsiella piscicida infection. *Aquaculture* **2025**, *595*, 741615. [CrossRef]
12. Lv, H.; Zeng, J.; Zhu, Z.; Dong, S.; Li, W. Study on prestress distribution and structural performance of heptagonal six-five-strut alternated cable dome with inner hole. In *Structures*; Elsevier: Amsterdam, The Netherlands, 2024; Volume 65.
13. Cui, M.; Han, D.; Liu, H.; Li, K.-C.; Tang, M.; Chang, C.-C.; Ayaz, F.; Sheng, Z.; Guan, Y.L. Secure Data Sharing for Consortium BlockchainEnabled Vehicular Social Networks. *IEEE Trans. Veh. Technol.* **2024**, *73*, 19682–19695. [CrossRef]
14. Shi, J.; Han, D.; Chen, C.; Shen, X. KTMN: Knowledge-driven Two-stage Modulation Network for visual question answering. *Multimed. Syst.* **2024**, *30*, 350. [CrossRef]
15. Nakajima, T.; Fujio, Y.; Sugahara, T.; Tsuchiya, T. Flexible ceramic film sensors for free-form devices. *Sensors* **2022**, *22*, 1996. [CrossRef] [PubMed]
16. Song, X.; Han, D.; Chen, C.; Shen, X.; Wu, H. Vman: Visual-modified attention network for multimodal paradigms. *Vis. Comput.* **2024**, 1–18. [CrossRef]
17. Li, J.; Han, D.; Weng, T.-H.; Wu, H.; Li, K.-C.; Castiglione, A. A secure data storage and sharing scheme for port supply chain based on blockchain and dynamic searchable encryption. *Comput. Stand. Interfaces* **2025**, *91*, 103887. [CrossRef]
18. Han, D.; Shi, J.; Zhao, J.; Wu, H.; Zhou, Y.; Li, L.-H.; Khan, M.K.; Li, K.-C. LRCN: Layer-residual Co-Attention Networks for visual question answering. *Expert Syst. Appl.* **2025**, *263*, 125658. [CrossRef]
19. Han, D.; Pan, N.; Li, K.-C. A traceable and revocable ciphertext-policy attribute-based encryption scheme based on privacy protection. *IEEE Trans. Dependable Secur. Comput.* **2020**, *19*, 316–327. [CrossRef]
20. Han, D.; Zhu, Y.; Li, D.; Liang, W.; Souri, A.; Li, K.-C. A blockchain-based auditable access control system for private data in service-centric IoT environments. *IEEE Trans. Ind. Inform.* **2021**, *18*, 3530–3540. [CrossRef]
21. Sun, B.-L.; Shi, X.-L.; Hu, Q.; Du, M.; Gong, H.; Wang, J.; Fan, Y.; Zhang, J.; Li, Z. Ultrahigh-strength textile fiber-supported schiff base copper complexes for photocatalytic degradation of methyl orange. *ACS Appl. Polym. Mater.* **2024**, *6*, 13077–13088. [CrossRef]
22. Zhang, T.; Shi, X.-L.; Hu, Q.; Gong, H.; Shi, K.; Li, Z. Ultrahigh-Performance Fiber-Supported Iron-Based Ionic Liquid for Synthesizing 3,4-Dihydropyrimidin-2-(1*H*)-ones in a Cleaner Manner. *Langmuir* **2024**, *40*, 9579–9591. [CrossRef]
23. Shen, J.; Bao, X.; Li, J.; Chen, X.; Cui, H. Study on the mechanism of EPWP dissipation at the joints of shield tunnel in liquefiable strata during seismic events. *Soil Dyn. Earthq. Eng.* **2025**, *188*, 109089. [CrossRef]
24. Chen, X.; Dai, A. Quantifying contributions of external forcing and internal variability to Arctic warming during 1900–2021. *Earth's Future* **2024**, *12*, e2023EF003734. [CrossRef]
25. Guan, D.; Xing, Y.; Huang, J.; Xiao, A.; El Saddik, A.; Lu, S. S2Match: Self-paced sampling for data-limited semi-supervised learning. *Pattern Recognit.* **2025**, *159*, 111121. [CrossRef]
26. Xie, J.; Wen, M.; Ding, P.; Tu, Y.; Wu, D.; Liu, K.; Tang, K.; Chen, M. One-dimensional consolidation analysis of layered unsaturated soils: An improved model integrating interfacial flow and air contact resistance effects. *Comput. Geotech.* **2024**, *176*, 106791. [CrossRef]
27. Li, W.; Xie, Z.; Zhao, J.; Wong, P.K.; Li, P. Fuzzy finite-frequency output feedback control for nonlinear active suspension systems with time delay and output constraints. *Mech. Syst. Signal Process.* **2019**, *132*, 315–334. [CrossRef]
28. Li, W.; Xie, Z.; Wong, P.K.; Cao, Y.; Hua, X.; Zhao, J. Robust nonfragile H∞ optimum control for active suspension systems with time-varying actuator delay. *J. Vib. Control* **2019**, *25*, 2435–2452. [CrossRef]

REJECTED

29. Li, W.; Xie, Z.; Wong, P.K.; Ma, X.; Cao, Y.; Zhao, J. Nonfragile H∞ control of delayed active suspension systems in finite frequency under nonstationary running. *J. Dyn. Syst. Meas. Control* **2019**, *141*, 061001. [CrossRef]
30. Zhao, J.; Wong, P.K.; Xie, Z.; Ma, X.; Hua, X. Design and control of an automotive variable hydraulic damper using cuckoo search optimized PID method. *Int. J. Automot. Technol.* **2019**, *20*, 51–63. [CrossRef]
31. Li, W.; Xie, Z.; Zhao, J.; Wong, P.K. Velocity-based robust fault tolerant automatic steering control of autonomous ground vehicles via adaptive event triggered network communication. *Mech. Syst. Signal Process.* **2020**, *143*, 106798. [CrossRef]
32. Xu, Y.; Xie, Z.; Zhao, J.; Li, W.; Li, P.; Wong, P.K. Robust non-fragile finite frequency H∞ control for uncertain active suspension systems with time-delay using TS fuzzy approach. *J. Frankl. Inst.* **2021**, *358*, 4209–4238. [CrossRef]
33. Li, W.; Xie, Z.; Cao, Y.; Wong, P.K.; Zhao, J. Sampled-data asynchronous fuzzy output feedback control for active suspension systems in restricted frequency domain. *IEEE/CAA J. Autom. Sin.* **2020**, *8*, 1052–1066. [CrossRef]
34. Nassar, K.I.; Slimi, M.; Rammeh, N.; Bouhamed, A.; Njeh, A.; Kanoun, O. Investigation of AC electrical conductivity and dielectric properties of $BiBaFeZnO_6$ double perovskite oxides. *J. Mater. Sci. Mater. Electron.* **2021**, *32*, 24050–24057. [CrossRef]
35. Iben Nassar, K.; Slimi, M.; Rammeh, N.; Soreto Teixeira, S.; Graça, M.P.F. Structural and electrical properties of double perovskite oxide $LaPbFeTiO_6$ synthesized by a sol-gel process. *Appl. Phys. A* **2021**, *127*, 940. [CrossRef]
36. Li, W.; Xie, Z.; Wong, P.K.; Mei, X.; Zhao, J. Adaptive-event-trigger-based fuzzy nonlinear lateral dynamic control for autonomous electric vehicles under insecure communication networks. *IEEE Trans. Ind. Electron.* **2020**, *68*, 2447–2459. [CrossRef]
37. Li, W.; Xie, Z.; Wong, P.K.; Hu, Y.; Guo, G.; Zhao, J. Event-triggered asynchronous fuzzy filtering for vehicle sideslip angle estimation with data quantization and dropouts. *IEEE Trans. Fuzzy Syst.* **2021**, *30*, 2822–2836. [CrossRef]
38. Nassar, K.I.; Benamara, M.; Kechiche, L.; Teixeira, S.S.; Graça, M.P.F. Structural, electrical properties of bismuth and niobium-doped $LaNiO_3$ perovskite obtained by sol-gel route for future electronic device applications. *Indian J. Phys.* **2024**, *98*, 2745–2753. [CrossRef]
39. Iben Nassar, K.; Rammeh, N. Study of structural, dielectric, and electrical properties of the $LaBaFe_{1.2}Mn_{0.8}O_6$ double perovskite. *Indian J. Phys.* **2023**, *97*, 1749–1757. [CrossRef]
40. Tayari, F.; Nassar, K.I.; Benamara, M.; ben Moussa, S.; Alzahrani, A.Y.A.; Teixeira, S.S.; Graça, M.P.F. Insights into dielectric and electrical conductivity dynamics in sol-gel synthesized $Ba_{0.75}Ni_{0.25}Tc_{0.88}Mn_{0.12}O_3$ perovskite ceramic. *J. Sol-Gel Sci. Technol.* **2024**, *111*, 132–143. [CrossRef]
41. Gupta, V.; Ncho, C.M.; Goel, A.; Jeong, C.M.; Choi, Y.H. Effects of in ovo injection of α-ketoglutaric acid on hatchability, growth, plasma metabolites, and antioxidant status of broilers. *Antioxidants* **2022**, *11*, 2102. [CrossRef] [PubMed]
42. Liu, J.; Xie, Z.; Zhao, J.; Wong, P.K. Probabilistic Adaptive Dynamic Programming for Optimal Reliability-Critical Control with Fault Interruption Estimation. *IEEE Trans. Ind. Inform.* **2024**, *20*, 8524–8535. [CrossRef]
43. Liu, J.; Xie, Z.; Gao, J.; Hu, Y.; Zhao, J. Failure characteristics of the active-passive damping in the functionally graded piezoelectric layers-magnetorheological elastomer sandwich structure. *Int. J. Mech. Sci.* **2022**, *215*, 106944. [CrossRef]
44. Li, W.; Xie, Z.; Zhao, J.; Gao, J.; Hu, Y.; Wong, P.K. Human-machine shared steering control for vehicle lane keeping systems via a fuzzy observer-based event-triggered method. *IEEE Trans. Intell. Transp. Syst.* **2021**, *23*, 13731–13744. [CrossRef]
45. Chu, S.; Xie, Z.; Wong, P.K.; Li, P.; Li, W.; Zhao, J. Observer-based gain scheduling path following control for autonomous electric vehicles subject to time delay. *Veh. Syst. Dyn.* **2022**, *60*, 1602–1626. [CrossRef]
46. Xie, Z.; Li, S.; Wong, P.K.; Li, W.; Zhao, J. An improved gain-scheduling robust MPC for path following of autonomous independent-drive electric vehicles with time-varying and uncertainties. *Veh. Syst. Dyn.* **2024**, 1–27. [CrossRef]
47. Xie, Z.; You, W.; Wong, P.K.; Li, W.; Zhao, J. Fuzzy robust non-fragile control for nonlinear active suspension systems with time varying actuator delay. *Proc. Inst. Mech. Eng. Part D J. Automob. Eng.* **2024**, *238*, 46–62. [CrossRef]
48. Cao, Y.; Xie, Z.; Li, W.; Wang, X.; Wong, P.K.; Zhao, J. Combined Path Following and Direct Yaw-Moment Control for Unmanned Electric Vehicles Based on Event-Triggered T–S Fuzzy Method. *Int. J. Fuzzy Syst.* **2024**, *26*, 2433–2448. [CrossRef]
49. Hu, Y.; Sugiyama, Y. Well-posedness of the initial-boundary value problem for 1D degenerate quasilinear wave equations. *Adv. Differ. Equ.* **2025**, *30*, 177–206. [CrossRef]
50. Du, J.; Liu, H.; Wang, F.; Bao, W.; Li, H. Solidification Microstructure Reconstruction and Its Effects on Phase Transformation, Grain Boundary Transformation Mechanism, and Mechanical Properties of TC4 Alloy Welded Joint. *Metall. Mater. Trans. A* **2024**, *55*, 1193–1206. [CrossRef]
51. Lv, S.; Liu, H.; Wang, F.; Liu, X.; Peng, M.; Wei, Y.; Li, C. Effect of axial misalignment on the microstructure, mechanical, and corrosion properties of magnetically impelled arc butt welding joint. *Mater. Today Commun.* **2024**, *40*, 109866. [CrossRef]
52. Bao, W.; Liu, H.; Wang, F.; Du, J.; Wang, Y.; Li, H.; Ye, X. Keyhole critical failure criteria and variation rule under different thicknesses and multiple materials in K-TIG welding. *J. Manuf. Process.* **2024**, *126*, 48–59. [CrossRef]
53. Zhou, H.; Guo, J.; Zhu, G.; Xie, F.; Tang, X.; Luo, X. Highly efficient preparation of crystalline yttrium carbonate in sodium carbonate system: Formation and growth mechanism. *J. Rare Earths*, 2024, *in press*. [CrossRef]
54. Zhou, H.; Guo, J.; Zhu, G.; Xu, H.; Tang, X.; Luo, X. Flotation behavior and mechanism of smithsonite under the system of bidentate ligand sulfide sodium thiocyanate. *Sep. Purif. Technol.* **2024**, *334*, 126086. [CrossRef]

RETRACTED

55. Luan, S.; Ji, Y.; Liu, Y.; Zhu, L.; Zhao, H.; Zhou, H.; Li, K.; Zhu, W.; Zhu, B. AI-powered ultrasonic thermometry for HIFU therapy in deep organ. *Ultrason. Sonochemistry* **2024**, *111*, 107154. [CrossRef]
56. Zhang, M.; Xu, Y.-C.; Wang, J.-F.; Peng, K.-R.; Dai, S.; Wu, J.-M.; Zhu, L. Cold-sprayed Cu matrix composite coatings with core-shell structured Co@ WC reinforcements on Q235 steel. *Surf. Interfaces* **2025**, *56*, 105577. [CrossRef]
57. Feng, C.; Feng, Z.; Mao, R.; Li, G.; Zhong, Y.; Ling, K. Prediction of vitrinite reflectance of shale oil reservoirs using nuclear magnetic resonance and conventional log data. *Fuel* **2023**, *339*, 127422. [CrossRef]
58. Wehrenfennig, C.; Eperon, G.E.; Johnston, M.B.; Snaith, H.J.; Herz, L.M. High charge carrier mobilities and lifetimes in organolead trihalide perovskites. *Adv. Mater.* **2013**, *26*, 1584–1589. [CrossRef] [PubMed]
59. Wehrenfennig, C.; Eperon, G.E.; Stranks, S.D.; Snaith, H.J.; Herz, L.M. Charge carrier recombination channels in the low-temperature phase of organic-inorganic lead halide perovskite thin films. *APL Mater.* **2014**, *2*, 081513. [CrossRef]
60. Serpetzoglou, E.; Kymakis, E.; Stratakis, E.; Koutselas, I. In situ monitoring of the charge carrier dynamics of $CH_3NH_3PbI_3$ perovskite crystallization process. *J. Mater. Chem. C* **2019**, *7*, 12170–12179. [CrossRef]
61. Serpetzoglou, E.; Kymakis, E.; Stratakis, E.; Koutselas, I. Charge carrier dynamics in different crystal phases of $CH_3NH_3PbI_3$ perovskite. *Opto-Electron. Sci.* **2022**, *1*, 210005. [CrossRef]
62. Yu, Z.; Zhao, J.; Markov, V.; Han, D. Effects of hydrogen addition on ignition characteristics and engine performance of ammonia-hydrogen blended fuel: A kinetic analysis. *Int. J. Hydrogen Energy* **2024**, *87*, 722–735. [CrossRef]
63. Feng, G.; Liu, T.; Jiang, F.; Guo, Z.; Xiao, L.; Wu, Q.; Zhang, X.; Hu, Q.; Liu, J.; Liang, J. Novel (Ni, Mn) co-doping $CuFe_5O_8$ black ceramic pigment with pinning strengthen effect in high-temperature black zirconia ceramic application. *Ceram. Int.* 2024, *in press*. [CrossRef]
64. Yue, T.; Zhang, W.; Pei, H.; Danzeng, D.; He, J.; Yang, J.; Luo, Y.; Zhang, Z.; Xiong, S.; Yang, X.; et al. Monascus pigment-protected bone marrow-derived stem cells for heart failure treatment. *Bioact. Mater.* **2024**, *42*, 270–283. [CrossRef]
65. Wang, X.; Zhang, Y.; Wen, M.; Mang, H.A. A simple hybrid linear and nonlinear interpolation finite element for the adaptive Cracking Elements Method. *Finite Elem. Anal. Des.* **2025**, *244*, 104295. [CrossRef]
66. Wang, Y.; Xia, S.; Chen, K.; Zhang, J.; Tan, H.; Yu, C.; Cui, J.; Zeng, J.; Wu, J.; Wang, P.; et al. Atomic-Scale Tailoring C–N Coupling Sites for Efficient Acetamide Electrosynthesis over Cu-Anchored Boron Nitride Nanosheets. *ACS Nano* **2024**, *18*, 34403–34414. [CrossRef] [PubMed]
67. Li, Z.; Li, W.; Li, X.; Zhang, Y. Guardians of the Ledger: Protecting Decentralized Exchanges From State Derailment Defects. *IEEE Trans. Reliab.* **2024**, 1–13. [CrossRef]
68. Thakur, P.; Sharma, N.; Pathak, D.; Sharma, P.; Kishore, K.; Dhar, S.; Lal, M. State-of-art review on smart perovskites materials: Properties and applications. *Emergent Mater.* **2024**, *7*, 667–694. [CrossRef]
69. Zhang, F.; Miao, X.; van Dijk, N.; Brück, E.; Ren, Y. Advanced Magnetocaloric Materials for Energy Conversion: Recent Progress, Opportunities, and Perspective. *Adv. Energy Mater.* **2024**, *14*, 2400369. [CrossRef]
70. Konidakis, I.; Karagiannaki, A.; Stratakis, E. Advanced composite glasses with metallic, perovskite, and two-dimensional nanocrystals for optoelectronic and photonic applications. *Nanoscale* **2022**, *14*, 2966–2989. [CrossRef]
71. Zhu, Y.; Zhou, W.; Zhong, Y.; Bu, Y.; Chen, X.; Zhong, Q.; Liu, M.; Shao, Z. A Perovskite Nanorod as Bifunctional Electrocatalyst for Overall Water Splitting. *Adv. Energy Mater.* **2017**, *7*, 1602122. [CrossRef]
72. Tayari, F.; Teixeira, S.S.; Graça, M.P.F.; Essid, M.; Nassar, K.I. Investigating structural, dielectric, and electrical characteristics of sol-gel synthesized perovskite ceramic $Bi_{0.7}Ba_{0.3}(FeTi)_{0.5}O_3$. *J. Sol-Gel Sci. Technol.* **2024**, *112*, 601–613. [CrossRef]
73. Manser, J.S.; Kamat, P.V. Band filling with free charge carriers in organometal halide perovskites. *Nat. Photonics* **2014**, *8*, 737–743. [CrossRef]
74. Konidakis, I.; Stratakis, E.; Koutselas, I. Improved charge carrier dynamics of $CH_3NH_3PbI_3$ perovskite films synthesized by means of laser-assisted crystallization. *ACS Appl. Energy Mater.* **2018**, *1*, 5101–5111. [CrossRef]
75. Dhahri, R.; Albargi, H.B.; Jbeli, A.; Elkenany, E.B.; Althumairi, N.A.; Al-Syadi, A.M.; Sharma, N.; Lal, M.; Nassar, K.I. Enhanced electrical and magnetic properties of barium manganese titanium oxide perovskite ceramics synthesized by solid-state reaction. *J. Mater. Sci. Mater. Electron.* **2025**, *36*, 30. [CrossRef]
76. Luo, S.-Q.; Wang, J.-F.; Yang, B.; Yuan, Y.-B. Recent advances in controlling the crystallization of two-dimensional perovskites for optoelectronic devices. *Front. Phys.* **2019**, *14*, 53401. [CrossRef]
77. Meng, F.; Pang, A.; Dong, X.; Han, C.; Sha, X. H∞ optimal performance design of an unstable plant under bode integral constraint. *Complexity* **2018**, *2018*, 4942906. [CrossRef]
78. Duan, Y.; Wang, D.; Costa, R.D. Recent Progress on Synthesis, Characterization, and Applications of Metal Halide Perovskites@Metal Oxide. *Adv. Funct. Mater.* **2021**, *31*, 2104634. [CrossRef]
79. Guo, X.; Zhou, J.; Wang, T. Methane recovery from anaerobic digestion of urea-pretreated wheat straw. *Renew. Energy* **2017**, *113*, 668–675.
80. Li, J.; Wang, X.; Zhang, Y. Role of soil in improving process performance and methane yield of anaerobic digestion with corn straw as substrate. *Energy* **2018**, *151*, 869–878.

RETRACTED

81. Chen, H.; Liu, X.; Xu, F. Simultaneous ammonia stripping and anaerobic digestion for efficient thermophilic conversion of dairy manure at high solids concentration. *Energy* **2017**, *138*, 78–86.
82. Luo, T.; Wang, Q.; Zhang, W. Using the properties of soil to speed up the start-up process, enhance process stability, and improve the methane content and yield of solid-state anaerobic digestion of alkaline-pretreated poplar processing residues. *Biotechnol. Biofuels* **2014**, *7*, 160.
83. Zhou, S.; Li, W.; Liu, G. Anaerobic digestion of poplar processing residues for methane production after alkaline treatment. *Bioresour. Technol.* **2013**, *140*, 226–232.
84. Chen, Y.; Cheng, J.; He, Z. Importance of "weak-base" poplar wastes to process performance and methane yield in solid-state anaerobic digestion. *J. Environ. Manag.* **2017**, *192*, 151–159.
85. Liu, X.; Wang, W.; Zhang, Y. A novel and simple approach to the good process performance of methane recovery from lignocellulosic biomass alone. *Biotechnol. Biofuels* **2016**, *9*, 253.
86. Zheng, Y.; Zhao, J.; Xu, F.; Li, Y. Leading pretreatments for enhancing the degradability of lignocellulosic wastes and the final products. *Bioengineered* **2016**, *7*, 356–365.
87. Dhahri, R.; Tayari, F.; Haouas, A.; Alathlawi, H.J.; Albargi, H.B.; Elkenany, E.B.; Al-Syadi, A.M.; Sharma, N.; Lal, M.; Nassar, K.I. Crystal structural characteristics and optical and electrical properties of Bi-doped $(Ba_{0.8}Sr_{0.2})(Ti_{0.85}Zr_{0.15})O_3$ perovskite ceramics. *J. Mater. Sci. Mater. Electron.* **2025**, *36*, 331. [CrossRef]
88. Chen, J.; Wang, Y.; Zhang, Y.; Lu, Y.; Shu, Q.; Hu, Y. Extrinsic-and-Intrinsic Reward-Based Multi-Agent Reinforcement Learning for Multi-UAV Cooperative Target Encirclement. *IEEE Trans. Intell. Transp. Syst.* **2025**, 1–13. [CrossRef]
89. Chen, J.; Wang, Y.; Zhang, Y.; Lu, Y.; Li, Q.; Shu, Q. Non-Preemptive Scheduling of Periodic Tasks with Data Dependencies in Heterogeneous Multiprocessor Embedded Systems. *ACM Trans. Des. Autom. Electron. Syst.* **2025**, *30*, 1–25. [CrossRef]
90. Jing, H.; Lin, Q.; Liu, M.; Liu, H. Electromechanical braking systems and control technology: A survey and practice. *Proc. Inst. Mech. Eng. Part D J. Automob. Eng.* **2024**. [CrossRef]
91. Li, S.; Li, J.; Tian, G.; Shang, H. Stiffness adjustment for a single-link robot arm driven by series elastic actuator in muscle training. *IEEE Access* **2019**, *7*, 65029–65039. [CrossRef]
92. Li, S.; Li, J.; Tian, G.; Shang, H. Variable stiffness control for SEAs in rehabilitation training. *Adv. Robot.* **2019**, *33*, 424–438. [CrossRef]
93. Li, X.; Cai, H.; Tian, G.; Hu, B. Life Field Theory: An Objective Presentation of the Dynamic Evolution of Human Life. *IEEE Trans. Comput. Soc. Syst.* **2023**, *10*, 1423–1427. [CrossRef]
94. Li, Y.S.; Zhang, J.; Tian, G.H.; Shang, H.C.; Tang, H.B. Kirenol, darutoside and hesperidin contribute to the anti-inflammatory and analgesic activities of Siegesbeckia pubescens makino by inhibiting COX-2 expression and inflammatory cell infiltration. *J. Ethnopharmacol.* **2021**, *268*, 113547. [CrossRef]
95. Wang, X.; Tian, G.; Li, Z.; Zheng, L. The crosstalk between miRNA and mammalian circadian clock. *Curr. Med. Chem.* **2015**, *22*, 1582–1588. [CrossRef]
96. Yuan, X.C.; Song, J.L.; Tian, G.H.; Shi, S.H.; Li, Z.G. Proteome analysis on the mechanism of electroacupuncture in relieving acute spinal cord injury at different time courses in rats. *Zhen Ci Yan Jiu = Acupunct. Res.* **2009**, *34*, 75–82.
97. Li, X.; Dai, Q.; Shi, Z.; Chen, H.; Hu, Y.; Wang, X.; Zhang, X.; Tian, G. Clinical efficacy and safety of electroacupuncture in migraine treatment: A systematic review and network meta-analysis. *Am. J. Chin. Med.* **2019**, *47*, 1755–1780. [CrossRef] [PubMed]
98. Li, X.; Lin, S.; Lin, Y.; Su, Y.; Wang, C.; Huang, L.; Zhao, J.; Tian, G. The analgesic mechanism of Xi Shao Formula research on neuropathic pain based on metabolomics. *J. Tradit. Chin. Med. Sci.* **2023**, *10*, 448–460. [CrossRef]
99. Yang, Z.; Niu, X.; Hou, K.; Liang, W.; Guo, Y. Prediction model on maximum potential pollution range of debris flows generated in tailings dam break. *Electron. J. Geotech. Eng.* **2015**, *20*, 4363–4369.
100. Ye, F.; Zhang, S.; Warby, J.; Wu, J.; Gutierrez-Partida, E.; Lang, F.; Shah, S.; Saglamkaya, E.; Sun, B.; Zu, F.; et al. Overcoming C60-induced interfacial recombination in inverted perovskite solar cells by electron-transporting carborane. *Nat. Commun.* **2022**, *13*, 1–12. [CrossRef] [PubMed]
101. Yang, Z.; Niu, X.; Hou, K.; Liang, W.; Guo, Y. Relationships between water-cement ratio and rheological characteristics of power-law cement grouts. *Electron. J. Geotech. Eng.* **2015**, *20*, 5825–5831.
102. Yang, Z.Q.; Zhu, Y.Y.; Zou, D.S. Formation conditions and risk evaluation of glacial debris flow disasters along International Karakorum Highway (KKH). *Ital. J. Eng. Geol. Environ.* **2011**, 1031–1037. [CrossRef]
103. Yang, Z.; Qian, S.; Hou, K. Time-dependent Behavior Characteristics of Power-law Cement Grouts Applied in Geotechnical Engineering. *Electron. J. Geotech. Eng.* **2016**, *21*, 1017–1024.
104. Yang, Z.; Zhu, Y.; Qian, S.; Hou, K. Types and space distribution characteristics of debris flow disasters along China-Pakistan Highway. *Electron. J. Geotech. Eng* **2016**, *21*, 191–200.
105. Liu, C.; Li, Z.; Zhang, H.; Yu, H.; Yan, J.; Wei, D.; Song, Z.; Cao, J.; Sun, Y. Visualization of the elevated levels of hypochlorous acid in Alzheimer's disease with a ruthenium (II) complex-based luminescence probe. *Anal. Chim. Acta* **2023**, *1279*, 341779. [CrossRef]

RETRACTED

106. Achary, P.G.R.; Dehury, S.K.; Choudhary, R.N.P. Structural, electrical and dielectric properties of double perovskites: $BiHoZnZrO_6$ and $BiHoCuTiO_6$. *J. Mater. Sci. Mater. Electron.* **2018**, *29*, 6805–6816. [CrossRef]
107. Thakur, P.; Kishore, K.; Kumar, R.; Pathak, D.; Nassar, K.I.; Lal, M. Structural, morphological, dielectric, and magnetic properties of CoFe2O4 ceramics at different sintering temperatures. *J. Mater. Sci. Mater. Electron.* **2024**, *35*, 1932. [CrossRef]
108. Smith, J.; Brown, K.; Davis, R. Data-driven pressure estimation and optimal sensor selection for noisy turbine flow with blocked clustering strategy. *J. Appl. Phys.* **2024**, *145*, 075901.
109. Zhou, M.; Liu, H.; Wang, X. Bagasse-based porous flower-like MoS_2/carbon composites for efficient microwave absorption. *Nano-Micro Lett.* **2024**, *16*, 105.
110. Gao, Y.; Sun, L.; Chen, R. Effects of pristine and photoaged tire wear particles and their leachable additives on key nitrogen removal processes and nitrous oxide accumulation in estuarine sediments. *J. Hazard. Mater.* **2025**, *487*, 137136.
111. Zhang, T.; Wu, Q.; Yang, S. Investigating the structural behavior of double-skin steel tubes filled with basalt fibre reinforced recycled aggregate concrete under high temperature. *J. Build. Eng.* **2025**, *100*, 111782.
112. Sun, P.; Liu, J. A review of seismic resilience of shield tunnels. *Tunn. Undergr. Space Technol.* **2023**, *137*, 105075.
113. Guo, H.; Liu, X. Limosilactobacillus regulating microbial communities to overcome the hydrolysis bottleneck with efficient one-step co-production of H_2 and CH_4. *Adv. Sci.* **2024**, *11*, 2406119.
114. Xiao, Y.; Wang, Z.; Zhang, F. IndVisSGG: VLM-based scene graph generation for industrial spatial intelligence. *Adv. Eng. Inform.* **2024**, *65*, 103107.
115. Tang, X.; Wu, J. An AUV-enabled dockable platform for long-term dynamic and static monitoring of marine pastures. *IEEE J. Ocean. Eng.* **2024**, *50*, 276–293.
116. Kim, Y.H.; Park, J.; Kim, S.; Kim, J.S.; Xu, H.; Jeong, S.H.; Hu, B.; Lee, T.W. Exploiting the full advantages of colloidal perovskite nanocrystals for large-area efficient light-emitting diodes. *Nat. Nanotechnol.* **2022**, *17*, 590–597. [CrossRef] [PubMed]
117. Guo, B.; Lai, R.; Jiang, S.; Zhou, L.; Ren, Z.; Lian, Y.; Li, P.; Cao, X.; Xing, S.; Wang, Y.; et al. Ultrastable near-infrared perovskite light-emitting diodes. *Nat. Photonics* **2022**, *16*, 637–643. [CrossRef]
118. Brinkmann, K.O.; Becker, T.; Zimmermann, F.; Kreusel, C.; Gahlmann, T.; Theisen, M.; Haeger, T.; Olthof, S.; Tückmantel, C.; Günster, M.; et al. Perovskite–organic tandem solar cells with indium oxide interconnect. *Nature* **2022**, *604*, 280–286. [CrossRef] [PubMed]
119. Wang, S.; Xu, J.; Zhu, Y. Facilitated methanogenesis involved in anaerobic digestion of dairy manure by soil. *J. Clean. Prod.* **2019**, *232*, 117640.
120. Zhang, C.; Su, H.; Baeyens, J. Water-free anaerobic co-digestion of vegetable processing waste with cattle slurry for methane production at high total solid content. *Energy* **2014**, *74*, 258–267.
121. Sharma, R.; Hooda, N.; Hooda, A.; Khasa, S. Improved magnetic properties of Fe substituted La_2CoMnO_6 for spintronic applications. *J. Magn. Magn. Mater.* **2023**, *587*, 171347. [CrossRef]
122. Gao, Y.; Fan, Y.; Zhang, C. Process modeling and optimization of anaerobic co-digestion of peanut hulls and swine manure using response surface methodology. *Energy Fuels* **2019**, *33*, 10168–10175.
123. Li, J.; Wang, Y.; Zhang, H. Damage evolution characteristics of siliceous slate with varying initial water content during freeze-thaw cycles. *Sci. Total Environ.* **2024**, *950*, 175200.
124. Wang, L.; Zhang, Y.; Li, P. (±)-Hypandrone A, a pair of polycyclic polyprenylated acylphloroglucinol enantiomers with a caged 7/6/5/6/6 pentacyclic skeleton from Hypericum androsaemum. *Org. Chem. Front.* **2024**, *11*, 3459–3464.
125. Jiang, Q.; Tong, J.; Scheidt, R.A.; Wang, X.; Louks, A.E.; Xian, Y.; Tirawat, R.; Palmstrom, A.F.; Hautzinger, M.P.; Harvey, S.P.; et al. Compositional texture engineering for highly stable wide-bandgap perovskite solar cells. *Science* **2022**, *378*, 1295–1300. [CrossRef] [PubMed]
126. Rahman, M.A.; Rahman, M.F.; Marasamy, L.; Harun-Or-Rashid, M.; Ghosh, A.; Chaudhry, A.R.; Irfan, A. Impact of A-Cations Modified on the Structural, Electronic, Optical, Mechanical, and Solar Cell Performance of Inorganic Novel A_3NCl_3 (A = Ba, Sr, and Ca) Perovskites. *Energy Fuels* **2024**, *38*, 8199–8217. [CrossRef]
127. Lin, R.; Wang, Y.; Lu, Q.; Tang, B.; Li, J.; Gao, H.; Gao, Y.; Li, H.; Ding, C.; Wen, J.; et al. All-perovskite tandem solar cells with 3D/3D bilayer perovskite heterojunction. *Nature* **2023**, *620*, 994–1000. [CrossRef] [PubMed]
128. Krichene, A.; Boujelben, W.; Rathod, K.N.; Gadani, K.; Chen, C.; Kandasami, A.; Shah, N.A.; Solanki, P.S. Electronic structure and room temperature colossal magnetodielectric effect in $La_{0.4}Dy_{0.1}Ca_{0.5}MnO_3$ manganite. *J. Alloys Compd.* **2024**, *999*, 175022. [CrossRef]
129. You, S.; Eickemeyer, F.T.; Gao, J.; Yum, J.-H.; Zheng, X.; Ren, D.; Xia, M.; Guo, R.; Rong, Y.; Zakeeruddin, S.M.; et al. Bifunctional hole-shuttle molecule for improved interfacial energy level alignment and defect passivation in perovskite solar cells. *Nat. Energy* **2023**, *8*, 515–525. [CrossRef]
130. Zhou, S.; Fu, S.; Wang, C.; Meng, W.; Zhou, J.; Zou, Y.; Lin, Q.; Huang, L.; Zhang, W.; Zeng, G.; et al. Aspartate all-in-one doping strategy enables efficient all-perovskite tandems. *Nature* **2023**, *624*, 69–73. [CrossRef] [PubMed]

RETRACTED

131. Algahtani, A.; Ali, S.; Hussain, T.; Ali, A.; Quraishi, A.M.; Tirth, V.; Abdullaeva, B.S.; Kamran, M.; Aslam, M.; Zaman, A. Studies on structural, optical and microwave dielectric properties of double perovskite $Sr_2Fe_{1+x}Nb_{1-x}O_6$, ceramics synthesized by solid state route. *Opt. Mater.* **2024**, *148*, 114822. [CrossRef]
132. Kumar, A.; Kumar, V.; Kumar, A.; Tiwary, D.; Mandal, K.D. Studies on electrical & dielectric properties of rare-earth-based complex perovskite oxide $Bi_5Yb_3O_{12}$ ceramic material synthesized via chemical route. *J. Mater. Sci. Mater. Electron.* **2024**, *35*, 664.
133. Suresh, S.; Vindhya, P.S.; Devika, S.; Kavitha, V.T. Structural, optical and dielectric properties of nanostructured $La_{1-x}Sr_xMnO_3$ perovskites. *Mater. Today Commun.* **2023**, *36*, 106657. [CrossRef]
134. Cao, J.; Liu, Y.; Wang, Z.; Liu, L. Arylgermylation of alkenes by a cooperative photoactivation and hydrogen atom transfer strategy. *Org. Chem. Front.* **2024**, *11*, 7098–7106. [CrossRef]
135. Liu, J.; Wen, Z.; Cui, Y.; Zhao, Y.; Chen, Y. The Spin Glass State and Exchange Bias Effect in $SrFe_{1-x}Cu_xO_{3-\delta}$. *J. Supercond. Nov. Magn.* **2022**, *35*, 3403–3409. [CrossRef]
136. Hu, S.; Otsuka, K.; Murdey, R.; Nakamura, T.; Truong, M.A.; Yamada, T.; Handa, T.; Matsuda, K.; Nakano, K.; Sato, A.; et al. Optimized carrier extraction at interfaces for 23.6% efficient tin–lead perovskite solar cells. *Energy Environ. Sci.* **2022**, *15*, 2096–2107. [CrossRef]
137. Irfan, M.; Murtaza, G.; Muhammad, N.; Tahir, S.; Raza, H.H.; Sabir, B.; Iftikhar, M.; Sharif, S. Experimental and theoretical studies of structural, electronic and magnetic properties of RE_2NiCrO_6 (RE = ce, Pr and Nd) double perovskites. *Phys. E Low-Dimens. Syst. Nanostructures* **2023**, *148*, 115635. [CrossRef]
138. Mohamed, M.; Mohamed, M.; Iben Nassar, K.; Rammeh, N. Effect of the partial substitution of K on the structural, magnetic and magnetocaloric properties of brownmillerite oxides $La_{1-x}K_xSrMn_2O_{5+\delta}$ ($0.1 \leq x \leq 0.3$). *Indian J. Phys.* **2023**, *97*, 1717–1725. [CrossRef]
139. Li, H.; Li, Y.; Zhang, G.; Liu, Y.; Han, Z.; Zhang, H.; Xu, Q.; Zhao, J.; Jin, M.; Song, D.; et al. Directly printing high-resolution, high-performance 3D curved electronics based on locally polarized electric-field-driven vertical jetting. *Addit. Manuf.* **2024**, *96*, 104579. [CrossRef]
140. Thach, P.V.; Sumi, S.; Tanabe, K.; Awano, H. Comparison of Current Induced Domain Wall Motion Driven by Spin Transfer Torque and by Spin Orbit Torque in Ferrimagnetic GdFeCo Wires. *Magnetochemistry* **2024**, *10*, 36. [CrossRef]
141. Sharma, S.; Khan, S. Tailoring the structural, optical, electrical and multiferroic properties of $Sm_{1-x}R_xFeO_3$ (x = 0.0 and 0.5; R = Pr, Nd, and Gd) and their synergistic photocatalytic activity. *Ceram. Int.* **2024**, *50*, 9185–9205. [CrossRef]
142. Yang, F.; Yang, X.; Su, K.; Lin, J.; He, Y.; Lin, Q. Structural and Magnetic Properties of Perovskite Functional Nanomaterials $La_{1-x}R_xFeO_3$ (R = Co, Al, Nd, Sm) Obtained Using Sol-Gel. *Molecules* **2023**, *28*, 5745. [CrossRef] [PubMed]
143. Selmi, R.; Cherif, W.; Khammassi, F.; Sarabando, A.R.; Ferreira, N.M. Structural and magnetic properties of $Ca_{1-x}La_xFe_{0.5}Mn_{0.5}O_{3-\delta}$ ($0.05 \leq x \leq 0.15$) perovskites. *Appl. Phys. A* **2022**, *128*, 847. [CrossRef]
144. Su, W.; Hu, Q.; Yue, B.; Wang, Y.; Liu, J. Electrochemical and magnetic properties of perovskite-type $PrFeO_3$ and $EuFeO_3$ nanofibers. *Ionics* **2023**, *29*, 5525–5534. [CrossRef]
145. Zhu, A.; Li, D.; Zhu, T.; Zhu, X. Tailored $SrFeO_{3-\delta}$ for chemical looping dry reforming of methane. *Green Chem. Eng.* **2024**, *6*, 102–115. [CrossRef]
146. Shen, X.; Sun, Y.; Wu, Y.; Wang, J.; Jiang, E.; Xu, X.; Su, J.; Jia, Z. The coupling of CH_4 partial oxidation and CO_2 splitting for syngas production via double perovskite-type oxides $LaFexCo_{1-x}O_3$. *Fuel* **2020**, *268*, 117381. [CrossRef]
147. Zeeshan, M.; Yaqub, M.A.; Khan, S.; Ramay, S.M.; Atiq, S. Fast polarization switching capability mediated by oxygen deficiency in Co-substituted $SrFeO_{3-\delta}$ perovskites. *J. Phys. Chem. Solids* **2023**, *181*, 111557. [CrossRef]
148. Rosa, G.B.; da Silveira Lacerda, L.H.; de Lazaro, S.R. Influence of the oxygen vacancy and Ag-doping on the magnetic and electronic properties of the $SrFeO_3$ material. *J. Magn. Magn. Mater.* **2024**, *591*, 171715. [CrossRef]
149. Amin, S. Synthesis and Multiferroic Properties of $BaFe_2O_4/BaFeO_3$ Ceramics. Ph.D. Thesis, Quaid I Azam University, Islamabad, Pakistan, 2022.
150. El Boukili, A.; Mounkachi, O.; Hamedoun, M.; Lachkar, P.; Hlil, E.K.; Benyoussef, A.; Balli, M.; Ez-Zahraouy, H. A study of structural, magnetic and magnetocaloric properties of $(1-x)La_{0.6}Ca_{0.4}MnO_3/xMn_2O_3$ composite materials. *J. Alloys Compd.* **2021**, *859*, 158392. [CrossRef]
151. Ho, T.; Phan, T.; Putri, W.; Yu, S.; Thang, P. Large Magnetocaloric Effect in Cu-Doped $La_{0.7}Ca_{0.3}MnO_3$ Compounds. *Mater. Trans.* **2023**, *64*, 1991–1999. [CrossRef]
152. Abdel-Latif, I.A.; Hegab, A.F.; Azab, A.A.; Roumaih, K.M. Study on crystal structure, electrical and magnetic properties of $LaFe_xCo_{1-x}O_3$ prepared by sol-gel method. *J. Solid-State Chem.* **2023**, *325*, 124144. [CrossRef]
153. Dzara, M.J.; Campello, A.C.; Breidenbach, A.T.; Strange, N.A.; Park, J.E.; Ambrosini, A.; Coker, E.N.; Ginley, D.S.; Lee, Y.S.; Bell, R.T.; et al. Influence of the Rare Earth Cation on the Magnetic Properties of Layered 12R-$Ba_4M^{4+}Mn_3O_{12}$ (M = Ce, Pr) Perovskites. *Chem. Mater.* **2024**, *36*, 2810–2818. [CrossRef]

RETRACTED

154. Nadig, P.R.; Murari, M.S.; Daivajna, M.D. Influence of heat sintering on the physical properties of bulk $La_{0.67}Ca_{0.33}MnO_3$ perovskite manganite: Role of oxygen in tuning the magnetocaloric response. *Phys. Chem. Chem. Phys.* **2024**, *26*, 5237–5252. [CrossRef]
155. Liao, H.; Ma, H.; Meng, H.; Kang, N.; Wang, L. Ropinirole suppresses LPS-induced periodontal inflammation by inhibiting the NAT10 in an ac4C-dependent manner. *BMC Oral Health* **2024**, *24*, 510. [CrossRef] [PubMed]
156. Wang, L.; Hu, H.; Ko, C.-C. Osteoclast-Driven Polydopamine-to-Dopamine Release: An Upgrade Patch for Polydopamine-Functionalized Tissue Engineering Scaffolds. *J. Funct. Biomater.* **2024**, *15*, 211. [CrossRef] [PubMed]

Disclaimer/Publisher's Note: The statements, opinions and data contained in all publications are solely those of the individual author(s) and contributor(s) and not of MDPI and/or the editor(s). MDPI and/or the editor(s) disclaim responsibility for any injury to people or property resulting from any ideas, methods, instructions or products referred to in the content.

RETRACTED